Simultaneous-Approximation-Term based Boundary Discretization for Moment Equations of Rarefied Gas Dynamics

Neeraj Sarna*, Harshit Kapadia, Manuel Torrilhon

Center for Computational Engineering & Department of Mathematics
RWTH Aachen University, Germany
sarna@mathcces.rwth-aachen.de, harshit.kapadia@rwth-aachen.de,
mt@mathcces.rwth-aachen.de

Abstract

Previous works have developed boundary conditions that lead to the L^2-boundedness of solutions to the linearised moment equations. Here we present a spatial discretization that preserves the L^2-stability by recovering integration-by-parts over the discretized domain and by imposing boundary conditions using a simultaneous-approximation-term (SAT). We develop three different forms of the SAT using: (i) characteristic splitting of moment equation's boundary conditions; (ii) decoupling of moments in moment equations; and (iii) characteristic splitting of Boltzmann equation's boundary conditions. We discuss how the first two forms differ in terms of their usage and implementation. We show that the third form is equivalent to using an upwind kinetic numerical flux along the boundary, and we argue that even though it provides stability, it prescribes the incorrect number of boundary conditions. Using benchmark problems, we compare the accuracy of moment solutions computed using different SATs. Our numerical experiments also provide new insights into the convergence of moment approximations to the Boltzmann equation's solution.

1. Introduction

The Boltzmann equation (BE) governs the evolution of a phase density functional and accurately describes gas flows for all thermodynamic regimes. Although Monte-Carlo methods provide a flexible framework for solving the BE [5], they suffer from sampling noise, motivating one to look for deterministic Galerkin methods that approximate BE's solution in a finite-dimensional space [9, 14, 30, 43]. In the present work, we also use a Galerkin method where along the velocity domain we approximate the solution in the span of Grad's Hermite polynomials, and along the spatial domain we use a finite element approximation [14].

For initial boundary value problems (IBVPs), a Hermite expansion requires boundary conditions. These boundary conditions first appeared in Grad's work [14] however, at least for linearised moment equations, they lead to L^2-instabilities [32]; instabilities prohibit an a-priori convergence analysis and can lead to inaccurate results [29, 45]. For the first time in [37] authors proposed boundary conditions for the regularised-13 (R13) moment equations that lead to its L^2-stability. Furthermore, authors in [29, 36] showed enhanced physical accuracy of these stable R13 equations and recently [32, 33] authors developed L^2-stable Grad's moment approximations of (formally) arbitrary order. Extensions to multi-physics problems can also be found in [4, 36].

All of the above works focused on ensuring a L^2-bound for the solution on a spatially continuous level. In the present work, we develop a finite element (FE) approximation that preserves the L^2-stability of a moment approximations on a spatially discrete level. Such a FE approximation requires an appropriate discretization of boundary conditions, and the present literature offers

two possible ways to do so. Either one can include boundary conditions in the solution space of the FE approximation, or one can include boundary conditions into the variational formulation and approximate them along with the solution through a simultaneous-approximation-term (SAT) [10, 25, 27, 39]. For hyperbolic equations, a SAT offers comparatively easy implementation and leads to provably stable numerical schemes when coupled with a spatial discretization that recovers a discrete analogue of integration-by-parts. See the review papers [12, 40] for a comprehensive survey of such stable schemes. Since linearised Grad's moment equations are hyperbolic, we include boundary conditions in a FE approximation through a SAT. To recover integration-by-parts on a spatially discrete level, we assume the exact integration of volume integrals involving divergences. Since we use linearised moment equations, we justify the assumption of exact integration with the use of a sufficient number of quadrature points.

A SAT requires a well-defined penalty matrix, and we present the following three different variants of this penalty matrix: (i) characteristic penalty matrix that uses characteristic splitting of moment equation's boundary conditions; (ii) odd penalty matrix that uses the decoupling of moments in moment equations; and (iii) kinetic penalty matrix that uses the characteristic splitting of BE's boundary conditions. Authors in [25] proposed the first form of the penalty matrix whereas the other two forms are a novelty of the present work. Using benchmark problems, we compare the physical accuracy of solutions computed using different SATs. To quantify physical accuracy, we use the L^2-error in macroscopic quantities, and we perform all our experiments on a bounded two-dimensional domain. Although some works [9, 28] have studied the physical accuracy of moment approximations on two-dimensional domains, ours is the first that studies convergence by comparing the moment solution to the discrete velocity solution [24].

For solutions that are continuously differentiable in space and time, we show that a kinetic penalty matrix imposes the incorrect number of boundary conditions that leads to non-physical oscillations in numerical experiments. Given our negative results for a kinetic penalty matrix, our motivation behind discussing it is two-fold. Firstly, it is intuitive to use an upwind kinetic numerical flux to prescribe boundary conditions for moment equations and for that reason, several previous works have proposed it [1, 22, 23, 41]. Here we show that using an upwind kinetic flux is equivalent to using a SAT with a kinetic penalty matrix. Secondly, as to our knowledge, in the context of well-posedness, such a boundary discretization is not analysed before. Assuming continuous differentiability of the solution, we present such an analysis and show that the number of boundary conditions prescribed by an upwind kinetic flux is inconsistent with the moment equations.

The type of spatial discretization one uses is problem-dependent. Owing to a square domain discretized with a Cartesian grid, and smooth solutions, we use a continuous Galerkin (CG) based spatial discretization. For problems with discontinuous solutions, one would use a discontinuous Galerkin (DG) framework. Moreover, for spatial domains with more than two dimensions, both CG and DG discretizations, when coupled with a velocity domain discretization, might lead to a very large number of degrees of freedom resulting in an unaffordable computation. See [44] for an explicit expression for the degrees of freedom resulting from a Grad's Hermite expansion. In such a case, one can reduce the number of degrees of freedom, while retaining accuracy, through an adaptive velocity domain discretization. For adaptivity and coupling of moment equations, DG provides greater flexibility as compared to CG [1]. Note that the treatment of boundary conditions in a DG framework (or any other SBP type scheme) is possible through the same SAT we develop here.

We first develop our FE approximation for a general linear first-order IBVP that has assumptions upon its structure. We then show that the linearised Grad's moment equations, P_3 equations of radiation transport, and the two-dimensional wave equation, are included in our general framework. Work done in [17, 36] indicates that moment equations resulting from binary gas mixtures and evaporation are also a special case of our general framework but a rigorous

investigation is needed.

2. General Framework

We consider a general linear first-order IBVP, and using an odd and a characteristic penalty matrix, we formulate a stable semi-discrete FE approximation for the same. Later, we discuss particular IBVPs that are special cases of our general formulation. The FE approximation involving kinetic penalty matrix requires an introduction to the BE, and we discuss it later.
A general first-order IBVP is given as

$$\partial_t \alpha + \sum_{i=1}^{d} A^{(i)} \partial_{x_i} \alpha = P\alpha, \text{ in } \Omega \times [0,T], \quad \alpha(t=0) = \alpha_I, \text{ on } \Omega, \quad B\alpha = \mathcal{G}, \text{ on } \partial\Omega \times [0,T], \quad (1)$$

where $\Omega \subset \mathbb{R}^d$ $(1 \leq d \leq 3)$ is bounded and polyhedral, and $x \in \mathbb{R}^d$ denotes a spatial coordinate. We denote the solution vector by $\alpha(x,t) \in \mathbb{R}^n$, and $A^{(i)} \in \mathbb{R}^{n\times n}$ is a constant matrix. The constant matrix $P \in \mathbb{R}^{n\times n}$ scales the reaction term, and the initial data is given by $\alpha_I(x) \in \mathbb{R}^n$. The matrix $B(x) \in \mathbb{R}^{p\times n}$ prescribes boundary conditions, and $\mathcal{G}(x,t) \in \mathbb{R}^p$ is a known solution independent vector containing boundary inhomogeneities. For simplicity, we assume that B is x-dependent, including t-dependence at the expense of some technical complications is trivial. The value of p governs the total number of prescribed boundary conditions, and we specify it later.

For stability analysis, we make the following regularity assumption on the initial and boundary data.

Assumption 1. *We assume that $\alpha_I \in L^2(\Omega;\mathbb{R}^n)$ and $\mathcal{G} \in L^2(\partial\Omega \times [0,T];\mathbb{R}^p)$.*

Assumption 2. *Assumptions on the different matrices appearing in the IBVP are as follows.*

1. *We assume that all the matrices $A^{(i)}$ are symmetric i.e.,*

$$A^{(i)} = \left(A^{(i)}\right)^{\mathrm{T}} \quad \forall \quad i \in \{1,\dots,d\}, \quad (2)$$

   where $(.)^{\mathrm{T}}$ denotes the transpose of a matrix.

2. *We assume that $A^{(1)}$ has the structure*

$$A^{(1)} = \begin{pmatrix} 0_{p\times p} & \tilde{A} \\ \left(\tilde{A}\right)^{\mathrm{T}} & 0_{q\times q} \end{pmatrix}, \quad (3)$$

   where $\tilde{A} \in \mathbb{R}^{p\times q}$, $p \leq q$ and $p+q=n$. Note that this p is the same p that defines the number of rows of B, reason for this similarity will be clear later. With $0_{q\times q}$ (and $0_{p\times p}$) we denote a zero matrix of size $q \times q$ (and $p \times p$).

3. *We assume that $\tilde{A}$ has full rank*

$$\operatorname{rank}\left(\tilde{A}\right) = p. \quad (4)$$

   Since by previous assumption we have $p \leq q$, the above condition is equivalent to all the rows of $\tilde{A}$ begin linearly independent.

4. *Let $x \in \partial\Omega$, and let $n(x) \in \mathbb{R}^d$ be a unit vector that is perpendicular to $\partial\Omega$ at the point x. We assume that $n(x)$ points out of the domain Ω. Using $n(x)$ we define the matrix*

$$A^n := \sum_{i=1}^{d} A^{(i)} n_i(x). \tag{5}$$

We assume that there exists an orthogonal matrix ω^n (dependent on the unit normal $n(x)$) such that A^n is a similarity transform of $A^{(1)}$ under ω^n

$$A^n = (\omega^n)^{\mathrm{T}} A^{(1)} \omega^n, \quad \forall \quad n(x) \in \mathbb{R}^d. \tag{6}$$

In the context of moment equations, the above property is referred to as rotational invariance [45].

5. *We assume that the matrix P is negative semi-definite*

$$\alpha^{\mathrm{T}} P \alpha \leq 0, \quad \forall \quad \alpha \in \mathbb{R}^n.$$

For convenience, we define the following.

Definition 2.1. *With $EV\,(A)_-$ we represent the total number of negative eigenvalues of a matrix $A \in \mathbb{R}^{n\times n}$.*

Using assumption 2, we can show that [33]

$$EV\left(A^{(1)}\right)_- = EV\,(A^n)_- = p, \quad \forall \quad n(x) \in \mathbb{R}^d. \tag{7}$$

The above relation is equivalent to the claim that at every point along the boundary $\partial\Omega$, the system in (1) has p number of incoming characteristics. Therefore, we can prescribe a set of boundary conditions to only the incoming characteristics through a boundary matrix (B) of the form [32, 33]

$$B(x) = B^{(1)}(x)\omega^n \quad \text{where} \quad B^{(1)}(x) = \left(I_{p\times p}, -R(x)\tilde{A}\right), \quad \forall \quad x \in \partial\Omega. \tag{8}$$

Above, $R(x) \in \mathbb{R}^{p\times p}$ is *s.p.d* for all $x \in \partial\Omega$, and $I_{p\times p}$ is an identity matrix of size $p \times p$. Here and elsewhere, *s.p.d* is an abbreviation for a symmetric positive definite matrix. With the above set of boundary conditions, we arrive at the following bound for the IBVP's solution [29, 32]

$$\|\alpha(\cdot, T)\|^2_{L^2(\Omega;\mathbb{R}^n)} \leq C(T, \alpha_I, \mathcal{G}), \tag{9}$$

where $C(T, \alpha_I, \mathcal{G}) \in \mathbb{R}^+$ is $(T, \alpha_I, \mathcal{G})$-dependent[1]. In the following sections we develop a semi-discrete FE approximation that preserves the above stability estimate on a spatially discrete level. Note that the specific form of the boundary matrix (i.e., the one given in (8)) is not necessary for the above bound, indeed the boundary matrix resulting from the kinetic penalty matrix (discussed later) will not have the form in (8). However, to prescribe boundary conditions to the incoming characteristics, if one assumes that $B(x) = (I_{p\times p}, L(x))$, with $L(x) \in \mathbb{R}^{p\times q}$, then the above abound is attained if and only if $L(x) = -R(x)\tilde{A}$. The details of this result are given in [32].

[1]For further discussion, $C(T, \alpha_I, \mathcal{G}) \in \mathbb{R}^+$ will denote a $(T, \alpha_I, \mathcal{G})$-dependent constant, new factors might be included in $C(T, \alpha_I, \mathcal{G})$ without a change in notation

Remark 1. *Explicit form of the matrix $R(x)$ depends upon the physical system that the IBVP models. For example, consider the wave equation (see example 2.1) for which $R(x)$ can depend on the reflection coefficient of a surface. Similarly for moment equations, in case of a gas-wall interaction, $R(x)$ depends upon the wall's roughness [29, 33].*

Remark 2. *Since in (2) we assume that $A^{(i)}$ is symmetric, the system in (1) is symmetric hyperbolic and the bound in (9) signifies its entropy stability. See [19] for a discussion on symmetric hyperbolic equations, and their entropy functions.*

Remark 3. *For linear IBVPs, the fact that the boundary matrix in (8) prescribes boundary conditions to only the incoming characteristics and that it leads to the bound in (9), is equivalent to the IBVP being well-posedness[18, 21, 26].*

2.1 Finite Element Approximation: Boundary Discretization Let $\Omega_h = \{\kappa\}$ denote a shape regular discretization of Ω. We assume that elements of Ω_h intersect only at sets of measure zero in $\mathbb{R}^d$ and that the intersection between two elements is the face of both the elements. Moreover, we assume that each element κ is a bijective image of a reference element $\hat{\kappa}$ i.e., $\kappa = F_\kappa(\hat{\kappa})$ with F_κ being a κ-dependent bijective mapping. The reference element $(\hat{\kappa})$ could either be a unit simplex or a unit hypercube in $\mathbb{R}^d$. With h_κ we represent the diameter of an element κ and we parametrise the triangulation through one representative diameter $h = \max_{\kappa\in\Omega_h}(h_\kappa)$. Using Ω_h, we define our FE approximation space of continuous functions as

$$V_h := \{v \in \left[C^0(\Omega_h)\right]^n \ : \ v|_\kappa \circ F_\kappa \in [P_1(\hat{\kappa})]^n \ , \ \forall\, \kappa \in \Omega_h\}, \tag{10}$$

where $P_1(\hat{\kappa})$ is a space of linear (or bilinear) polynomials defined over $\hat{\kappa}$. To approximate our IBVP (1), we project it onto V_h that provides a FE approximation given as

$$\begin{aligned}
&\text{find } \alpha_h(t) \in V_h \text{ such that} \\
&\int_{\Omega_h} \phi^{\mathrm{T}} \partial_t \alpha_h(t) dx + \sum_{i=1}^{d} \int_{\Omega_h} \phi^{\mathrm{T}} A^{(i)} \partial_{x_i} \alpha_h(t) dx \\
&\qquad = \int_{\Omega_h} \phi^{\mathrm{T}} P \alpha_h(t) dx + \underline{\oint_{\partial\Omega_h} \phi^{\mathrm{T}} \Sigma \left(B\alpha_h(t) - \mathcal{G}(t)\right) ds}, \quad \forall\, \phi \in V_h,\ \forall\, t \in [0,T] \\
&\int_{\Omega_h} \phi^{\mathrm{T}} \alpha_h(t=0) dx = \int_{\Omega_h} \phi^{\mathrm{T}} \alpha_I dx,\ \forall\, \phi \in V_h.
\end{aligned} \tag{11}$$

Above, dependencies on x are suppressed for brevity, and $\Sigma \in \mathbb{R}^{n\times p}$ is a penalty matrix that we define later. For further discussion we assume that the solution to the above variational form is continuously differentiable in time. We summarise our assumption in the following.

Assumption 3. *We assume that $\alpha_h(x,\cdot) \in \left[C^1([0,T])\right]^n$ for all $x \in \Omega_h$.*

Rather than including boundary conditions in the approximation space V_h, we included them in the variational form through the underlined term. Since the underlined term approximates the boundary conditions simultaneously with the solution, it is referred to as the simultaneous-approximation-term (SAT) [10, 12]. The SAT leads to a numerical solution that might not satisfy the boundary conditions exactly or so-called strongly, and therefore such a boundary implementation is referred to as the weak boundary implementation [40]. Through the penalty matrix Σ, the SAT penalizes the inability of the numerical solution in strongly satisfying the boundary conditions, and at least formally one expects the deviation $B\alpha_h - \mathcal{G}$ to tend to zero (in some norm) as the grid is refined [40, 46].

It is favourable to have a FE approximation that is L^2-stable and mimics the bound on the exact solution (9). Precisely speaking, we want the FE solution to satisfy

$$\|\alpha_h(\cdot,T)\|^2_{L^2(\Omega;\mathbb{R}^n)} \leq C(T,\alpha_I^h,\mathcal{G}^h), \tag{12}$$

where α_I^h and $\mathcal{G}^h$ are some numerical approximations to the initial and boundary data, respectively. For the above bound we require integration-by-parts and an appropriately defined penalty matrix [10, 20]. Integration-by-parts follows by assuming that the integrals $\int_{\Omega_h} \phi^{\mathrm{T}} A^{(i)} \partial_{x_i} \alpha_h(t) dx$ and $\int_{\Omega_h} (\partial_{x_i}\phi)^{\mathrm{T}} A^{(i)} \alpha_h(t) dx$ are exact, that provides

$$\sum_{i=1}^{d} \int_{\Omega_h} \left(\phi^{\mathrm{T}} A^{(i)} \partial_{x_i} \alpha_h(t) + (\partial_{x_i}\phi)^{\mathrm{T}} A^{(i)} \alpha_h(t) \right) dx = \oint_{\partial\Omega_h} \phi^{\mathrm{T}} A^n \alpha_h(t) ds. \tag{13}$$

All the above terms are polynomials in x, thus a use of sufficient number of quadrature points ensures exact integration.

Apart from integration-by-parts, for stability, we need to define the penalty matrix Σ. Below we introduce two different penalty matrices, both of which lead to stability. The characteristic penalty matrix is well-known in the literature (see [25, 45] and references therein) and results from expressing the boundary conditions in terms of characteristic variables. The other penalty matrix is motivated by the structure of $A^{(1)}$ given in (3), and we label it as the odd penalty matrix Σ_o. The terminology will be clear when we introduce moment equations.

Characteristic Penalty Matrix: Since A^n (given in (6)) is symmetric, we decompose it as $A^n = X_n \lambda_n (X_n)^{\mathrm{T}}$ where X_n is an orthogonal matrix containing all the eigenvectors of A^n, and λ_n is a diagonal matrix containing all the eigenvalues of A^n. Similar to X_n, let X_n^- be a matrix that collects all the eigenvectors of A^n corresponding to negative eigenvalues. Moreover, let $|\lambda_n|$ be the same as λ_n but with all the diagonal entries of λ_n replaced by their absolute values. Using $|\lambda_n|$, we define $|A^n|$ as $|A^n| = X_n |\lambda_n| (X_n)^{\mathrm{T}}$ and using $|A^n|$, we give the characteristic penalty matrix as

$$\Sigma_c(x) = \frac{1}{2} \left(A^n - |A^n|\right) X_n^- \left(B(x) X_n^-\right)^{-1}, \quad \forall \quad x \in \partial\Omega. \tag{14}$$

Replacing Σ by Σ_c in the FE formulation (11) and using integration-by-parts (13), one can shown that the FE formulation is stable (12). Detailed derivation of Σ_c and its stability proof can be found in [25].

Using the rotational invariance of the matrix A^n given (6), we simplify the above expression for Σ_c. We collect all eigenvectors of $A^{(1)}$ in X_1, and we collect all eigenvectors of $A^{(1)}$ corresponding to negative eigenvalues in X_1^-. Rotational invariance of A^n implies that $X_n = (\omega^n)^{\mathrm{T}} X_1$ and $X_n^- = (\omega^n)^{\mathrm{T}} X_1^-$. Using these relations, the explicit expression for the matrix $B(x)$ from (8) and the rotational invariance property of A^n, we arrive at a simpler expression for Σ_c

$$\Sigma_c(x) = \frac{1}{2} (\omega^n)^{\mathrm{T}} \left(A^{(1)} - |A^{(1)}|\right) X_1^- \left(B^{(1)}(x) X_1^-\right)^{-1}, \quad \forall \quad x \in \partial\Omega. \tag{15}$$

As compared to (14), the above expression for Σ_c is simpler because it requires an eigenvalue decomposition of the matrix $A^{(1)}$, which is independent of the unit normal $n(x)$. In all our numerical experiments, we use the above form on Σ_c.

Odd Penalty Matrix: While formulating the characteristic penalty matrix, we neither exploit the structure of the matrix $A^{(1)}$ given in (3) nor of $B(x)$ given in (8). Below we present the odd penalty matrix that exploits the structure of both of these matrices and as a result, has

a simpler expression than Σ_c. We first give the odd penalty matrix and later elaborate on its differences from a characteristic one. The odd penalty matrix is given as

$$\Sigma_o(x) = (\omega^n)^{\mathrm{T}} \begin{pmatrix} 0_{p\times p} \\ \left(\tilde{A}\right)^{\mathrm{T}} \end{pmatrix}, \quad \forall \quad x \in \partial\Omega, \tag{16}$$

where $\tilde{A} \in \mathbb{R}^{p\times q}$ is defined in (3). Following result shows that with Σ replaced by Σ_o, the semi-discrete FE approximation in (11) is stable. The result relies on using the *s.p.d* nature of the matrix $R(x)$ appearing (8), and the structure of $A^{(1)}$ given in (3).

Lemma 2.1. *With Σ replaced by Σ_o, the semi-discrete FE approximation (11) satisfies the stability estimate*

$$\|\alpha_h(\cdot,T)\|^2_{L^2(\Omega;\mathbb{R}^n)} \leq C(T,\alpha^h_I,\mathcal{G}^h).$$

Proof. See appendix A. □

2.2 Discussion Based upon different criterion, we compare the two penalty matrices Σ_c and Σ_o.

Generality of usage: Proving stability with characteristic penalty matrix necessarily requires: (i) Jacobians ($A^{(i)}$) that are simultaneously symmetrizable; (ii) boundary conditions that prescribe a value to the incoming characteristics; and (iii) a bounded solution to the IBVP. However, apart from these three requirements, it does not require any other assumption made on the matrices $A^{(i)}$, neither does it require the specific form of the boundary matrix in (8). Being independent of these assumptions, one can use a characteristic penalty matrix for a broad range of linear IBVPs. Note that as mentioned in remark 3, requirement (ii) and (iii) is equivalent to the IBVP being well-posed.

Both the explicit form of the odd penalty matrix and the stability proof (given in lemma 2.1) rely on the structure of the matrix $A^{(i)}$ (given in (3), (6) and (4)), and of the boundary matrix given in (8). This restricts the use of an odd penalty matrix to systems that satisfy these assumptions. Examples of such systems are the wave equation (see example 2.1), and the linearised Grad's moment equations (see section 3). Presently, the P_N equations of radiation transport (see [6] for details of P_N equations) do not have boundary conditions that lead to a bounded solution, neither is it proven that P_N equations satisfy assumption 2. However, computationally we observe that at least till $N = 100$, P_N equations satisfy assumption 2 and appendix B shows this for $N = 3$. Based on this observation we speculate that for an arbitrary value of $N \in \mathbb{N}$, the P_N equations should satisfy assumption 2. In such a case, boundary conditions of the form (8) should lead to stability of the P_N equations allowing one to use an odd penalty matrix. Note that even for $N > 100$ one can check that P_N equations satisfy assumption 2 but it does not prove the same for any $N \in \mathbb{N}$. As mentioned in the introduction, the work in [17, 36] indicates that an odd penalty matrix can also be used for linearised moment equations resulting from binary gas mixtures and multi-phase flows.

Implementation overhead: The shape of a domain's boundary $\partial\Omega$ is encoded in the normal vector $n(x)$. Therefore, the dependence of both the penalty matrices on the shape of $\partial\Omega$ is clear from their definitions itself. However, only the characteristic penalty matrix depends upon the boundary matrix $B(x)$ which results in a major difference between the implementation overhead of the two penalty matrices.

As an example consider gas-wall interaction where the boundary matrix B depends upon the wall's roughness [33]. If the wall's roughness varies along the boundary then the inverse

appearing in the characteristic penalty matrix (i.e. $(B(x)X_n^-)^{-1}$ in (15)) should be computed separately for every different boundary quadrature point whereas, an odd penalty matrix does not require such a computation. A similar situation can arise in multi-physics problems. For example consider gas confined in a square domain with two boundary faces being solid walls, one face being an evaporation type boundary (see [36] for details), and the last one being an inflow/outflow type boundary. Again, the characteristic penalty matrix requires the computation of a separate inverse for every different boundary face. To summarise, stronger the variation of B along the boundary more is the implementation overhead of a characteristic penalty matrix. Moreover, the implementation overhead increases for time-dependent boundary matrices.

In addition to being dependent upon the boundary matrix, the characteristic penalty matrix requires an eigenvalue decomposition whereas the odd penalty does not. However, for the simplified characteristic penalty matrix (15), eigenvalue decomposition is required only at the beginning of any computation.

Convergence behaviour and Physical accuracy: It is important to compare the discretization error generated by the two different penalty matrices (Σ_c and Σ_o) on the same grid (Ω_h). A comparison through a rigorous a-priori convergence analysis is beyond the scope of the present article. However, later we will make this comparison through numerical experiments.

Moment equations form a hierarchy of physical models that approximate the Boltzmann equation [2, 45]. Later through numerical experiments, we will compare the physical accuracy of moment solutions computed with the two different penalty matrices.

In the following, we consider an example that presents the above discussed penalty matrices for the 2D wave equation.

Example 2.1. *For a 2D wave equation, the matrices appearing in (1) are given as*

$$A^{(1)} = \begin{pmatrix} 0 & 1 & 0 \\ 1 & 0 & 0 \\ 0 & 0 & 0 \end{pmatrix}, \quad A^{(2)} = \begin{pmatrix} 0 & 0 & 1 \\ 0 & 0 & 0 \\ 1 & 0 & 0 \end{pmatrix}, \quad P = 0_{3\times 3}. \tag{17}$$

Both the above matrices are symmetric, $A^{(1)}$ satisfies the assumption in (3) with $\tilde{A} = (1, 0)$, and the values for p and q are 1 and 2, respectively. Moreover, the matrix A^n given in (5) satisfies

$$A^n = (\omega^n)^{\mathrm{T}} A^{(1)} \omega^n \quad \textit{with} \quad \omega^n = \begin{pmatrix} 1 & 0 & 0 \\ 0 & n_1(x) & n_2(x) \\ 0 & -n_2(x) & n_1(x) \end{pmatrix}, \ \forall\, n(x) \in \mathbb{R}^d.$$

The above relation is the rational invariance property defined in (6). One can check that $EV\left(A^{(1)}\right)_- = p = 1$ which, due to (7), implies $EV\left(A^n\right)_- = EV\left(A^{(1)}\right)_- = 1$. Therefore, along the boundary we prescribe only one boundary condition.

Let $\alpha = (\alpha_1, \alpha_2, \alpha_3)^T$ be the solution vector. One can show that boundary conditions of the following form prescribe a value to only the incoming characteristics

$$\alpha_1(x, t) = R(x)(n_1(x)\alpha_2(x, t) + n_2(x)\alpha_3(x, t)). \tag{18}$$

Above, $R(x) \in \mathbb{R}^+$ for all $x \in \partial\Omega$, and for simplicity we have considered zero boundary inhomogeneity i.e. $\mathcal{G} = 0_{3\times 1}$. Here the positive scalar $R(x)$ can encode, for e.g., the reflection coefficient of a boundary surface.

To see that the above boundary conditions lead to stability of the wave equation, we multiply the 2D wave equation with α^T, use the above matrices $A^{(i)}$, integrate over the domain $\Omega \times [0, T]$ and use Gauss-Theorem to find

$$\|\alpha(\cdot, T)\|^2_{L^2(\Omega;\mathbb{R}^3)} - \|\alpha_I\|^2_{L^2(\Omega;\mathbb{R}^3)} = -\oint_{\partial\Omega} \alpha^T A^n \alpha ds = -2 \oint \alpha_1(n_1\alpha_2 + n_2\alpha_3) ds.$$

Substituting wave equation's boundary conditions from (18) into the above relation, and using the positivity of R, we find the L^2-bound

$$\|\alpha(\cdot,T)\|^2_{L^2(\Omega;\mathbb{R}^3)} \leq \|\alpha_I\|^2_{L^2(\Omega;\mathbb{R}^3)}.$$

To get the boundary matrix $B(x)$, we express the boundary conditions in a matrix-vector product form to find

$$B(x) = (1, -R(x), 0)\,\omega^n = \left(1, -R(x)\tilde{A}\right)\omega^n, \quad \forall \quad x \in \partial\Omega.$$

Using the above boundary matrix $B(x)$ and the matrix $A^{(1)}$ from (17), in the definition of the characteristic penalty matrix Σ_c (given in (14)) and the odd penalty matrix Σ_o (given in (16)), we find

$$\Sigma_c(x) = \frac{1}{1+R(x)}\left(-1, n_1(x), n_2(x)\right)^{\mathrm{T}}, \quad \Sigma_o(x) = \left(0, n_1(x), n_2(x)\right)^{\mathrm{T}}, \quad \forall \quad x \in \partial\Omega.$$

Clearly, through the boundary normal $n(x)$, both the penalty matrices depend upon the shape of the boundary $\partial\Omega$ whereas only the characteristic penalty matrix Σ_c is $R(x)$-dependent.

3. Linearised Moment Equations

This sections shows how the linearised Grad's moment equations are a special case of our general framework. We first present the linearised BE.

3.1 The Linearised Boltzmann Equation Let $\bar{f} : \Omega \times [0,T] \times \mathbb{R}^d \to \mathbb{R}^+$, $(x,t,\xi) \mapsto \bar{f}(x,t,\xi)$, represent the phase density function of a mono-atomic gas. The variable $\xi \in \mathbb{R}^d$ denotes the velocity of a gas molecules. We assume that $\bar{f}$ is normalised such that its macroscopic moments, density ($\bar{\rho}$), mean flow velocity ($\bar{v}_i$), temperature in energy units ($\bar{\theta}$), stress tensor ($\bar{\sigma}_{ij}$), and heat flux ($\bar{q}_i$), are given as

$$\bar{\rho} = \int_{\mathbb{R}^d} \bar{f} d\xi, \quad \bar{\rho}\bar{v}_i = \int_{\mathbb{R}^d} \xi_i \bar{f} d\xi, \quad \bar{\rho}\bar{v}_i\bar{v}_i + d\bar{\rho}\bar{\theta} = \int_{\mathbb{R}^d} \xi_i\xi_i \bar{f} d\xi,$$
$$\bar{\sigma}_{ij} = \int_{\mathbb{R}^d} C_{<i}C_{j>} \bar{f} d\xi, \quad \bar{q}_i = \frac{1}{2}\int_{\mathbb{R}^d} C_i C_j C_j \bar{f} d\xi,$$

where $C_i = \xi_i - \bar{v}_i$ is the so-called peculiar velocity, the angular brackets denote the trace free part of a tensor, and repeated indices imply Einstein's summation convention. See [35] for a detailed discussion on tensors. For simplicity, we non-dimensionalise all quantities with appropriate powers of some reference density $\bar{\rho}_0$, temperature $\bar{\theta}_0$ and length scale L.

For low Mach number flows, we assume $\bar{f}$ to be a perturbation of a ground state f_0 i.e., $\bar{f} = f_0 + \epsilon f$ where ϵ is a smallness parameter and $f_0(\xi) = \exp\left(-\xi_i\xi_i/2\right)/\sqrt[d]{2\pi}$ is a ground-state Gaussian distribution function. Replacing the linearisation for $\bar{f}$ into the non-linear BE and ignoring terms of order higher than $\mathcal{O}(\epsilon)$, we find the governing equation for f [16]

$$\begin{gathered}\partial_t f + \xi_i \partial_{x_i} f = \frac{1}{\mathrm{Kn}} Q(f), \text{ in } \Omega \times [0,T] \times \mathbb{R}^d, \quad f(t=0) = f_I, \text{ on } \Omega \times \mathbb{R}^d, \\ f = f_{in}, \text{ on } [0,T] \times \partial\Omega^-,\end{gathered} \tag{19}$$

where f_I and f_{in} are some suitable initial and boundary data, respectively. Substituting the linearisation of $\bar{f}$ into the definition of the macroscopic moments, we find the following linearisation for the different macroscopic quantities

$$\bar{\rho} = 1 + \epsilon\rho, \quad \bar{v}_i = \epsilon v_i, \quad \bar{\theta} = 1 + \epsilon\theta, \quad \bar{\sigma}_{ij} = \epsilon\sigma_{ij}, \quad \bar{q}_i = \epsilon q_i. \tag{20}$$

We will refer to the quantities ρ, v_i, etc., as the deviations in the respective macroscopic quantities. For stability analysis, we make regularity assumptions on the initial and boundary data.

Assumption 4. *We assume that* $f_I \in L^2(\Omega \times \mathbb{R}^d, f_0^{-1})$ *and* $f_{in} \in L^2(\partial\Omega \times [0,T] \times \mathbb{R}^d, f_0^{-1})$.

The set $\partial\Omega^-$ in (19) collects all those points along $\partial\Omega \times \mathbb{R}^d$ that correspond to incoming molecular velocities, and is given as

$$\partial\Omega^- := \{(x,\xi) \in \partial\Omega \times \mathbb{R}^d \ : \ \xi_i n_i(x) < 0\},$$

where $n(x)$ is the unit vector defined in (5).

In (19), Q is a linearised collision operator that could be a linearisation of either the BGK operator, the Boltzmann operator or, any other non-linear operator that models collisions between gas molecules. See [11] for an explicit expression of different collision operators. Although for stability analysis the exact form of Q is not important, Q must satisfy the following dissipation property

$$\langle f, Q(f)\rangle_K \leq 0 \quad \forall \quad f \in K, \tag{21}$$

where K is a Hilbert space defined as

$$K := L^2(\mathbb{R}^d, f_0^{-1}), \quad \|r\|_K := \sqrt{\int_{\mathbb{R}^d} r^2 f_0^{-1} d\xi}, \quad \langle r, g\rangle_K := \int_{\mathbb{R}^d} r g f_0^{-1} d\xi. \tag{22}$$

One can prove that both the linearised BGK and the linearised Boltzmann operator satisfy the above dissipation property [11, 15]. The dissipation property in (21) signifies the entropy dissipation caused by inter-molecular collisions, and is equivalent to $-Q$ being lower semi-bounded on K. The factor Kn that scales the collision operator is the Knudsen number and results from the non-dimensionalisation of the BE.

3.2 Linearised moment equations

To give our moment approximation, we first define the notion of moments.

Moments and Hermite polynomials: We define tensorial Hermite polynomials as [8, 14]

$$\psi_{\beta^{(i)}}(\xi) := \prod_{p=1}^{d} He_{\beta_p^{(i)}}(\xi_p), \quad \beta^{(i)} := \left(\beta_1^{(i)}, \ldots, \beta_d^{(i)}\right), \quad \|\beta^{(i)}\|_{l^1} = m, \tag{23}$$

where $\beta^{(i)} \in \mathbb{N}^d$ is a multi-index, m is the so-called degree of the basis function and He_i is an i-th order Hermite polynomial which satisfies orthogonality and recursion

$$\frac{1}{\sqrt{2\pi}} \int_{\mathbb{R}} He_i(y)\, He_j(y) \exp\left(-\frac{y^2}{2}\right) dy = \delta_{ij} \quad \Rightarrow \quad \int_{\mathbb{R}^d} \psi_{\beta^{(k)}} \psi_{\beta^{(l)}} f_0 d\xi = \prod_{p=1}^{d} \delta_{\beta_p^{(k)} \beta_p^{(l)}} \tag{24a}$$

$$\sqrt{i+1} He_{i+1}(y) + \sqrt{i} He_{i-1}(y) = y He_i(y), \ \forall\, y \in \mathbb{R}. \tag{24b}$$

Through the following definition, we collect basis functions corresponding to a particular degree in a vector, and define the notion of moments.

Definition 3.1. *Let* $n(m)$ *represent the total number of basis functions* $(\psi_{\beta^{(i)}}(\xi))$ *of degree* m *i.e.* $\|\beta^{(i)}\|_{l^1} = m$. *We collect all such basis functions in a vector* $\psi_m(\xi) \in \mathbb{R}^{n(m)}$. *Using* $\psi_m(\xi)$, *we define* $\lambda_m : K \to \mathbb{R}^{n(m)}$ *as* $\lambda_m(r) := \langle \psi_m f_0, r\rangle_K$, $\forall r \in K$. *Thus,* $\lambda_m(r)$ *represents a vector containing all the* m*-th order moments of* r.

We do the same as above for the even (and odd) basis functions and moments.

Definition 3.2. *Let $n_o(m)$ and $n_e(m)$ denote the total number of tensorial Hermite polynomials in $\psi_m(\xi)$ which are odd and even with respect to ξ_1, respectively. Correspondingly, let $\psi_m^o(\xi) \in \mathbb{R}^{n_o(m)}$ and $\psi_m^e(\xi) \in \mathbb{R}^{n_e(m)}$ represent vectors containing those basis functions, out of $\psi_m(\xi)$, which are odd and even with respect to ξ_1, respectively. Then, we define $\lambda_m^o : K \to \mathbb{R}^{n_o(m)}$ and $\lambda_m^e : K \to \mathbb{R}^{n_e(m)}$ as $\lambda_m^o(r) := \langle \psi_m^o f_0, r \rangle_K$, $\lambda_m^e(r) := \langle \psi_m^e f_0, r \rangle_K$ where $r \in K$.*

Now we define vectors which collect all the basis functions and moments upto a particular degree.

Definition 3.3. *To collect all the odd and even moments of $r \in K$ which have a degree less than or equal to M ($m \leq M$), we define*

$$\Psi_M^o(\xi) := \left(\psi_1^o(\xi)^{\mathrm{T}}, \psi_2^o(\xi)^{\mathrm{T}}, \dots, \psi_M^o(\xi)^{\mathrm{T}}\right)^{\mathrm{T}}, \quad \Psi_M^e(\xi) := \left(\psi_0^e(\xi)^{\mathrm{T}}, \psi_1^e(\xi)^{\mathrm{T}}, \dots, \psi_M^e(\xi)^{\mathrm{T}}\right)^{\mathrm{T}}$$
$$\Lambda_M^o(r) := \left(\lambda_1^o(r)^{\mathrm{T}}, \lambda_2^o(r)^{\mathrm{T}}, \dots, \lambda_M^o(r)^{\mathrm{T}}\right)^{\mathrm{T}}, \quad \Lambda_M^e(r) := \left(\lambda_0^e(r)^{\mathrm{T}}, \lambda_1^e(r)^{\mathrm{T}}, \dots, \lambda_M^e(r)^{\mathrm{T}}\right)^{\mathrm{T}}$$

where $\Lambda_M^o : K \to \mathbb{R}^{\Xi_o^M}$, $\Lambda_M^e : K \to \mathbb{R}^{\Xi_e^M}$, $\Psi_M^o(\xi) \in \mathbb{R}^{\Xi_o^M}$ and $\Psi_M^e(\xi) \in \mathbb{R}^{\Xi_e^M}$. We represent the total number of odd and even moments of degree less than or equal to M through $\Xi_o^M := \sum_{i=1}^M n_o(i)$ and $\Xi_e^M := \sum_{i=0}^M n_e(i)$ respectively. To collect all the moments of $r \in K$ which are of order less than or equal to M ($m \leq M$), we additionally define

$$\Psi_M(\xi) := \left(\Psi_M^o(\xi)^{\mathrm{T}}, \Psi_M^e(\xi)^{\mathrm{T}}\right)^{\mathrm{T}}, \quad \Lambda_M(r) := \left(\Lambda_M^o(r)^{\mathrm{T}}, \Lambda_M^e(r)^{\mathrm{T}}\right)^{\mathrm{T}}$$

where $\Psi_M(\xi) \in \mathbb{R}^{\Xi^M}$, $\Lambda_M : K \to \mathbb{R}^{\Xi^M}$ with $\Xi^M = \Xi_o^M + \Xi_e^M = \sum_{m=0}^M n(m)$.

Moment Equations: Following Grad's methodology [14], we approximate the solution to the linearised BE (given in (19)) through the series expansion

$$f(x,t,\xi) \approx f_M(x,t,\xi) = f_0(\xi) \sum_{m=0}^{M} \lambda_m(f_M(x,t,.)) \cdot \psi_m(\xi) = f_0(\xi) \left(\Lambda_M(f_M(x,t,.)) \cdot \Psi_M(\xi)\right). \tag{25}$$

To get the governing equation for $\Lambda_M(f_M(x,t,.))$, we test the linearised BE with $\Psi_M(\xi)$, integrate over the velocity space $\mathbb{R}^d$, and replace f by f_M to find [35]

$$\partial_t \Lambda_M(f_M(x,t,.)) + A_M^{(i)} \partial_{x_i} \Lambda_M(f_M(x,t,.)) = P_M \Lambda_M(f_M(x,t,.)), \ \forall\ (x,t) \in \Omega \times [0,T], \tag{26a}$$
$$\Lambda_M(f_M(x,t=0,.)) = \Lambda_M(f_I(x,.)), \quad \forall \quad x \in \Omega, \tag{26b}$$
$$B_M \Lambda_M(f_M(x,t,.)) = \mathcal{G}_M(x,t), \quad \forall \quad (x,t) \in \partial\Omega \times [0,T], \tag{26c}$$

where f_I is the initial data for the linearised BE, and the matrices $A_M^{(i)} \in \mathbb{R}^{\Xi^M \times \Xi^M}$ and $P_M \in \mathbb{R}^{\Xi^M \times \Xi^M}$, are given as

$$A_M^{(i)} = \left\langle \Psi_M f_0, \xi_i \left(\Psi_M\right)^{\mathrm{T}} f_0 \right\rangle_K, \quad P_M = \frac{1}{\mathrm{Kn}} \left\langle \Psi_M f_0, \left(Q\left(\Psi_M f_0\right)\right)^{\mathrm{T}} \right\rangle_K. \tag{27}$$

The value of M in (25) determines the formal accuracy of Grad's expansion along the velocity domain, with larger values of M leading to higher accuracy. We emphasise on the word formal here because, as $M \to \infty$, the moment approximation error (i.e. $\|f_M(\cdot,T,\cdot) - f(\cdot,T,\cdot)\|_{L^2(\Omega \times \mathbb{R}^d, f_0^{-1})}$) might not convergence to zero monotonically. Later, we will observe this non-monotonic convergence in our numerical results. Choosing different values of M results in a hierarchy of macroscopic models that converge to the BE, and by Chapman-Enskog expansion, one can show that for $M \geq 2$, all of these macroscopic models contain the linearised Euler and Navier-Stokes equations [31, 35].

The following discussion develops an explicit form for the matrix B_M by comparing the moment equations to the earlier discussed general framework.

Similarities to the general framework: We show that the linearised moment equations satisfy assumption 2, and thus are a special case of the general IBVP (1). For the result that follows, we will need the following rotational property of the basis functions

$$O^n_m \psi_m(O^n \xi) = \psi_m(\xi), \ \forall\, \xi \in \mathbb{R}^d,$$

where $O^n \in \mathbb{R}^{d\times d}$ is an orthogonal matrix, which rotates the Cartesian coordinates to the local coordinates defined by $n(x)$, and $O^n_m \in \mathbb{R}^{n(m)\times n(m)}$ is also an m and $n(x)$ dependent orthogonal matrix. A detailed derivation of this property can be found in [47] and references therein. Using Ψ_M from definition 3.3 and the above relation, it is trivial to conclude that

$$\hat{O}^n_M \Psi_M(O^n \xi) = \Psi_M(\xi), \tag{28}$$

where $\hat{O}^n_M \in \mathbb{R}^{\Xi^M\times\Xi^M}$ is an orthogonal matrix with different entries of O^n_m $(m \leq M)$ placed at appropriate locations. We will not need the explicit forms of O^n_m and $\hat{O}^n_M$, interested reader can find these explicit forms in [45].

The result given below shows that $A^{(1)}_M$ has the form

$$A^{(1)}_M = \begin{pmatrix} 0_{\Xi^M_o\times\Xi^M_o} & A^{(M,M)}_\Psi \\ \left(A^{(M,M)}_\Psi\right)^{\mathrm{T}} & 0_{\Xi^M_e\times\Xi^M_e} \end{pmatrix}, \tag{29}$$

which is similar to the one assumed in (3). Above, $0_{\Xi^M_o\times\Xi^M_o}$ is a zero matrix of size $\Xi^M_o \times \Xi^M_o$ and the matrix $A^{(M,M)}_\Psi$ is defined in the following.

Definition 3.4. *We define*

$$A^{(k,l)}_\psi := \left\langle \Psi^o_k f_0, \xi_1 \left(\psi^e_l\right)^{\mathrm{T}} f_0 \right\rangle_K, \quad A^{(k,l)}_\Psi = \left(A^{(k,0)}_\psi, A^{(k,1)}_\psi, \ldots, A^{(k,l)}_\psi\right),$$

where $A^{(k,l)}_\Psi \in \mathbb{R}^{\Xi^k_o\times\Xi^l_e}$ and $A^{(k,l)}_\psi \in \mathbb{R}^{\Xi^k_o\times n_e(l)}$. As is clear from the definition, $A^{(k,l)}_\psi$ is the inner product (in K) of the two vectors $\Psi^o_k(\xi) f_0(\xi)$ and $\xi_1 \psi^e_l(\xi) f_0(\xi)$. Moreover, $A^{(k,l)}_\psi$ are the different columns of $A^{(k,l)}_\Psi$.

The following result shows that the linearised moment system (26a) satisfies assumption 2. It is an extension of the results presented in [32, 33], and follows from a manipulation of inner products between Hermite polynomials. It extensively uses orthogonality between even and odd Hermite polynomials (24a), the recursion relation (24b) and the above mentioned rotational property of the basis. All of these properties are also satisfied by the spherical harmonics that are used to derive the P_N equations [6]. Therefore, we expect that a result of the following type must also hold true for the P_N equations. We hope to present such a result in our future work.

Lemma 3.1. *For the linearised moment equations given in (26a), following holds.*

1. *The matrices $A^{(i)}_M$, $i \in \{1, \ldots, d\}$, are symmetric.*
2. *The matrix $A^{(1)}_M$ given in (27) has the structure*

$$A^{(1)}_M = \begin{pmatrix} 0_{\Xi^M_o\times\Xi^M_o} & A^{(M,M)}_\Psi \\ \left(A^{(M,M)}_\Psi\right)^{\mathrm{T}} & 0_{\Xi^M_e\times\Xi^M_e} \end{pmatrix}. \tag{30}$$

3. *The matrix $A^{(M,M)}_\Psi$ is of full rank:* $\operatorname{rank}(A^{(M,M)}_\Psi) = \Xi^M_o$.

4. *Let $n(x) \in \mathbb{R}^d$ be the unit vector given in (6). Similar to A^n, define A_M^n as*

$$A_M^n := \sum_{i=1}^{d} A_M^{(i)} n_i(x). \tag{31}$$

Then, A_M^n is rotationally invariant i.e., $A_M^n = \left(\hat{O}_M^n\right)^{\mathrm{T}} A_M^{(1)} \hat{O}_M^n$ where $\hat{O}_M^n$ is the orthogonal matrix given in (28).

5. *The matrix P_M (27) is negative semi-definite.*

Proof. See appendix C. □

Boundary Conditions: Using the generic structure of the boundary matrix given in (8), we develop the boundary matrix B_M for the moment system. First, we compare our moment system (26a) to the general IBVP (1) which provides

$$\begin{gathered} p = \Xi_o^M, \quad q = \Xi_e^M, \quad \tilde{A} = A_\Psi^{(M,M)}, \quad EV\left(A_M^n\right)_- = EV\left(A_M^{(1)}\right)_- = \Xi_o^M, \ \forall\, n(x) \in \mathbb{R}^d, \\ n = p + q = \Xi_o^M + \Xi_e^M = \Xi^M, \quad \omega^n = \hat{O}_M^n. \end{gathered} \tag{32}$$

Using the above relations in the expression for the general boundary matrix (8), we find an explicit form of B_M

$$B_M(x) = \left(I_{\Xi_o^M \times \Xi_o^M}, -R_M A_\Psi^{(M,M)}\right) \hat{O}_M^n, \quad \forall \quad x \in \partial\Omega, \tag{33}$$

where $I_{\Xi_o^M \times \Xi_o^M} \in \mathbb{R}^{\Xi_o^M \times \Xi_o^M}$ is an identity matrix, $R_M \in \mathbb{R}^{\Xi_o^M \times \Xi_o^M}$ is a *s.p.d* matrix and $B_M(x) \in \mathbb{R}^{\Xi_o^M \times \Xi^M}$. The explicit form of R_M was developed in [32] and is given as

$$R_M = B_\Psi^{(M,M-1)} \left(A_\Psi^{(M,M-1)}\right)^{-1}, \tag{34}$$

where the matrix $B_\Psi^{(M,M-1)} \in \mathbb{R}^{\Xi_o^M \times \Xi_e^{M-1}}$ is given as

$$B_\Psi^{(M,M-1)} = 2 \int_{\mathbb{R}^{d-1}} \int_{\xi_1 > 0} \Psi_M^o \left(\Psi_{M-1}^e\right)^{\mathrm{T}} f_0 d\xi.$$

By definition, $B_\Psi^{(M,M-1)}$ is a weighted inner product of the odd and even basis functions along the half velocity space. Similar to $B_\Psi^{(M,M-1)}$, the boundary inhomogeneity $\mathcal{G}_M$ (26c) is a projection of the boundary data (f_{in}) onto the odd basis functions along the half velocity space and is given as [29, 33, 35]

$$\mathcal{G}_M(x,t) = \int_{\mathbb{R}^{d-1}} \int_{\xi_1 < 0} \Psi_M^o(\xi) f_{in}(x,t,\xi) d\xi, \quad \forall \quad (x,t) \in \partial\Omega \times [0,T]. \tag{35}$$

Remark 4. *The boundary matrix in (33) leads to the following desirable properties. Firstly, it leads to the well-posedness of the IBVP in (26a)-(26c) which results from the boundary matrix prescribing boundary conditions to the incoming characteristic and leading to a L^2-bound for the solution. Secondly, at least for a half-space spatial domain (i.e. $\Omega = (-\infty, 0) \times (-\infty, \infty) \times \ldots \times (-\infty, \infty)$), as $M \to \infty$, the moment system in (26a), along with the above boundary conditions, converges to the solution of the linearised BE in the L^2-sense [31]. Lastly, a Chapman-Enskog expansion of the boundary conditions leads to the boundary conditions of the Euler and Navier-Stokes equations, which is in agreement with the derivation of these macroscopic models from the BE [42].*

Any set of boundary conditions that provide the above three properties is acceptable, and it is not yet established that only the boundary matrix in (33) provides these properties.

3.3 Finite Element Approximation: Boundary Discretization As a result of lemma 3.1, a stable semi-discrete FE approximation for moment equations follows from the general formulation in (11), and is given as

$$\begin{aligned}
&\text{find } \Lambda_M(f_M^h(t)) \in V_h \text{ such that} \\
&\int_{\Omega_h} \phi^{\mathrm{T}} \partial_t \Lambda_M(f_M^h(t))dx + \sum_{i=1}^{d} \int_{\Omega_h} \phi^{\mathrm{T}} A_M^{(i)} \partial_{x_i} \Lambda_M(f_M^h(t))dx - \int_{\Omega_h} \phi^{\mathrm{T}} P_M \Lambda_M(f_M^h(t))dx \\
&\qquad = \oint_{\partial\Omega_h} \phi^{\mathrm{T}} \Sigma^M \left(B_M \Lambda_M(f_M^h(t)) - \mathcal{G}_M(t) \right) ds, \ \forall\, \phi \in V_h, \ \forall\, t \in [0,T], \\
&\int_{\Omega_h} \phi^{\mathrm{T}} \Lambda_M(f_M^h(t=0))dx = \int_{\Omega_h} \phi^{\mathrm{T}} \Lambda_M(f_I)dx, \ \forall\, \phi \in V_h.
\end{aligned} \tag{36}$$

Above we have suppressed dependencies on x and ξ for brevity. The penalty matrix Σ^M is either the characteristic penalty matrix (15) or the odd penalty matrix (16), both of which are given as

$$\begin{aligned}
\text{Characteristic Penalty:} \quad & \Sigma_c^M(x) = \frac{1}{2} \left(\hat{O}_M^n \right)^{\mathrm{T}} \left(A_M^{(1)} - |A_M^{(1)}| \right) X_M^- \left(B_M^{(1)}(x) X_M^- \right)^{-1}, \\
\text{Odd Penalty:} \quad & \Sigma_o^M(x) = \left(\hat{O}_M^n \right)^{\mathrm{T}} \begin{pmatrix} 0_{\Xi_o^M \times \Xi_o^M} \\ \left(A_\Psi^{(M,M)} \right)^{\mathrm{T}} \end{pmatrix}.
\end{aligned} \tag{37}$$

Above, $B_M^{(1)}(x) = \left(I_{\Xi_o^M \times \Xi_o^M}, -R_M A_\Psi^{(M,M)} \right)$, and we identify $B_M^{(1)}(x)$ by comparing general boundary matrix (8) with moment equation's boundary matrix (33). Moreover, $\hat{O}_M^n$ is the rotation matrix in (28), X_M^- contains all those eigenvectors of $A_M^{(1)}$ that correspond to its negative eigenvalues, and $A_\Psi^{(M,M)}$ is as given in definition 3.4.

3.4 Gas-wall interaction The BE's boundary conditions given in (19) are inflow-outflow type but in all our numerical experiments we will consider a fully accommodated wall boundary. For completeness, we show that such a wall boundary is included in our above framework. The details of our discussion are given in [14, 29, 32, 33]. We model the gas-wall interaction using Maxwell's accommodation model where the boundary data f_{in}, for a fully accommodated wall, reads

$$f_{in}(x,t,\xi) = \left(\rho^{in}(x,t) + v_i^{in}(x,t)\xi_i + \frac{\theta^{in}(x,t)}{2} \left(\xi_i \xi_i - 3 \right) \right) f_0(\xi). \tag{38}$$

Above, v^{in} and θ^{in} denote the deviations in a wall's velocity and temperature, respectively. Let $v_n = v_i n_i$ denote the normal wall velocity, we consider only those walls that have $v_n = 0$, and we compute ρ^{in} in terms of v^{in} and θ^{in} such that the normal velocity remains zeros. Physically, this is equivalent to ensuring that the net mass-flux across the wall is zero. An explicit expression for ρ^{in} can be found in several works, a few of which are [14, 28, 29].

Projecting Maxwell's accommodation model onto odd basis functions, and adjusting the coefficients of the highest order even moments provides the boundary conditions

$$B_M^{\text{wall}} \Lambda_M = \mathcal{G}_M^{\text{wall}} \quad \text{where} \quad B_M^{\text{wall}} = \left(I_{\Xi_o^M \times \Xi_o^M}, -R_M^{\text{wall}} A_\Psi^{(M,M)} \right) \hat{O}_M^n.$$

Above $A_\Psi^{(M,M)}$ is given in definition 3.4, and $\hat{O}_M^n$ is the rotation matrix in (28). Moreover, in contrast to the *s.p.d* matrix R_M given in (33), the matrix $R_M^{\text{wall}} \in \mathbb{R}^{\Xi_o^M \times \Xi_o^M}$ is only symmetric positive semi-definite. Semi-definiteness of R_M^{wall} leads to a L^2 bound for the moment solution

if and only if $\mathcal{G}_M^{\text{wall}} \in \text{range}(R_M^{\text{wall}})$. This condition holds true because R_M^{wall} and $\mathcal{G}_M^{\text{wall}}$ have the structure

$$R_M^{\text{wall}} = \begin{pmatrix} 0 & 0_{1\times(\Xi_o^M-1)} \\ 0_{(\Xi_o^M-1)\times 1} & \hat{R}_M^{\text{wall}} \end{pmatrix}, \quad \mathcal{G}_M^{\text{wall}} = \begin{pmatrix} 0 \\ \hat{\mathcal{G}}_M^{\text{wall}} \end{pmatrix},$$

where $\hat{R}_M^{\text{wall}}$ is *s.p.d.* This proves that with the gas-wall boundary conditions, a moment solution is bounded in L^2 and one can ensure stability on a spatially discrete level using the same framework as developed above.

4. Weak kinetic boundary discretization

In previous sections, we approximated the linearised BE in the following three steps. Firstly, we approximated f along the velocity space through the Hermite series expansion given in (25). Secondly, we equipped f_M with boundary conditions given in (33). Lastly, we approximated f_M along the spatial domain (Ω) through the FE approximation given in (36). Here we combine the first and the second step by defining a finite-dimensional space $V_{h,M}$ that combines the spatial and the velocity space approximation. We approximate the linearised BE by projecting it onto $V_{h,M}$ and with a SAT we impose boundary conditions of the linearised BE weakly hence the name, weak kinetic boundary discretization. In the sense of (12), we show that such a FE approximation is stable. Moreover, for classical continuously differentiable solutions, we argue that a weak kinetic boundary implementation prescribes the incorrect number of boundary conditions. The details are as follows.

To combine the spatial and the velocity space approximation, we include the velocity space approximation in V_h by defining

$$V_{h,M} := \{(\alpha(x) \cdot \Psi_M(\xi))\, f_0(\xi) \ : \ \alpha \in V_h\},$$

where V_h and Ψ_M are as given in (10) and definition 3.3, respectively. Trivially, $V_{h,M}$ is a finite dimensional subspace of the Hilbert space

$$X := L^2(\Omega \times \mathbb{R}^d, f_0^{-1}), \quad \|r\|_X := \sqrt{\int_\Omega \int_{\mathbb{R}^d} r^2 f_0^{-1} d\xi dx}, \quad \langle r, g\rangle_X := \int_\Omega \int_{\mathbb{R}^d} r g f_0^{-1} d\xi dx. \tag{39}$$

By projecting the linearised BE (19) onto $V_{h,M}$, we approximate its solution through the variational form

$$\begin{aligned}
&\text{find } f_M^h(t) \in V_{h,M} \text{ such that} \\
&\left\langle \phi, \partial_t f_M^h(t) \right\rangle_X + \left\langle \phi, \xi_i \partial_{x_i} f_M^h(t) \right\rangle_X \\
&\qquad = \frac{1}{\text{Kn}} \left\langle \phi, Q(f_M^h(t)) \right\rangle_X + \underline{\oint_{\partial\Omega_h} \int_{\mathbb{R}^d} \phi \Sigma_k \left(f_M^h(t) - f_{in}(t) \right) f_0^{-1} d\xi ds}, \ \forall\ \phi \in V_{h,M}, \ \forall\ t \in [0,T], \\
&\left\langle \phi, f_M^h(t=0) \right\rangle_X = \langle \phi, f_I \rangle_X, \quad \forall \quad \phi \in V_{h,M}.
\end{aligned} \tag{40}$$

Similar to (11), the underlined term imposes boundary conditions weakly, and we need an explicit expression for the scalar kinetic penalty matrix Σ_k. Since the linearised BE is symmetric hyperbolic, we get Σ_k by formulating a characteristic penalty matrix (i.e. Σ_c) for the linearised BE. First we identify different matrices appearing in the expression for Σ_c given in (14). Since $A^n = \xi_i n_i$ is a scalar, X_n^- is one. Moreover, the boundary matrix $B(x)$, for all $x \in \partial\Omega$, is also

one. Substituting the expression for A^n, $B(x)$ and X_n^- into the expression for Σ_c given in (14), we find[2]

$$\Sigma_k(x) = \frac{1}{2}\left(\xi_i n_i(x) - |\xi_i n_i(x)|\right), \quad \forall \quad x \in \partial\Omega. \tag{41}$$

For the above Σ_k, the following result establishes the stability of the variational form in (40).

Lemma 4.1. *Similar to assumption 3, assume that the solution to the semi-discrete FE approximation (40) is continuously differentiable in time*

$$f_M^h(x,\cdot,\xi) \in C^1([0,T]), \quad \forall \quad (x,\xi) \in \Omega \times \mathbb{R}^d.$$

Then, with Σ_k given by (41), the semi-discrete FE approximation (40) satisfies

$$\|f_M^h(\cdot,T,\cdot)\|_X^2 \leq C(T, f_I^h, f_{in}^h) \tag{42}$$

where f_I^h and f_{in}^h are some numerical approximations to f_I and f_{in}, respectively.

Proof. See appendix D. □

Remark 5. *Fundamentally, both Σ_c^M given in (37) and Σ_k given in (41) are characteristic penalty matrices. However, Σ_c^M uses characteristic splitting for moment equation's boundary conditions whereas Σ_k uses the same splitting for linearised BE's boundary conditions. For the same reason, only Σ_c^M is M-dependent.*

As to our knowledge, the variational form in (40) is not well-known whereas, the variational form involving an upwind kinetic numerical fluxes has received attention in the literature [1, 23, 41]. The following result establishes equivalence between the variational form in (40) and the one that uses upwind kinetic numerical fluxes along element boundaries.

Lemma 4.2. *The variational form in (40) is equivalent to*

$$\begin{aligned}
&\textit{find } \Lambda_M(f_M^h(t)) \in V_h \textit{ such that} \\
&\int_{\Omega_h} \phi^{\mathrm{T}} \partial_t \Lambda_M(f_M^h(t))dx + \sum_{\kappa\in\Omega_h} \int_{\partial\kappa} \phi^{\mathrm{T}} \mathcal{F}(\Lambda_M^{(\kappa,-)}, \Lambda_M^{(\kappa,+)}; n_\kappa) ds \\
&\qquad - \sum_{\kappa\in\Omega_h} \sum_{i=1}^{d} \int_\kappa (\partial_{x_i}\phi)^{\mathrm{T}} A_M^{(i)} \Lambda_M(f_M^h(t))dx = \int_{\Omega_h} \phi^{\mathrm{T}} P_M \Lambda_M(f_M^h(t))dx, \ \forall\, \phi \in V_h, \ \forall\, t \in [0,T], \\
&\int_{\Omega_h} \phi^{\mathrm{T}} \Lambda_M(f_M^h(t=0))dx = \int_{\Omega_h} \phi^{\mathrm{T}} \Lambda_M(f_I)dx, \ \forall\, \phi \in V_h,
\end{aligned} \tag{43}$$

where $\mathcal{F}(\Lambda_M^{(\kappa,+)}, \Lambda_M^{(\kappa,-)}; n_\kappa)$ is the upwind kinetic numerical flux given as

$$\mathcal{F}(\Lambda_M^{(\kappa,+)}, \Lambda_M^{(\kappa,-)}; n_\kappa) = \frac{A_M^{n_\kappa}}{2}\left(\Lambda_M^{(\kappa,+)} + \Lambda_M^{(\kappa,-)}\right) + \frac{D_M^{n_\kappa}}{2}\left(\Lambda_M^{(\kappa,+)} - \Lambda_M^{(\kappa,-)}\right),$$

$$D_M^{n_\kappa} := \int_{\mathbb{R}^d} \Psi_M |\xi \cdot n_\kappa| (\Psi_M)^{\mathrm{T}} f_0 d\xi.$$

[2] We can also recover an expression for Σ_k by comparing the linearised BE with a scalar advection equation given by $\partial_t u(x,t) + \beta_i \partial_{x_i} u(x,t) = 0$ where $\beta \in \mathbb{R}^d$ is a constant vector. Penalty matrix for the scalar advection equation is given as [40]

$$\Sigma(x) = \frac{1}{2}\left(\beta_i n_i(x) - |\beta_i n_i(x)|\right), \quad \forall \quad x \in \partial\Omega.$$

By identifying β as ξ we find (41).

Above in (43), $\partial\kappa$ denotes the boundary of an element κ. The unit vector $n_\kappa(x) \in \mathbb{R}^d$ points out of the domain and is perpendicular to an element's boundary at the point $x \in \partial\kappa$. The matrix $A_M^{n_\kappa}$ is the same as A_M^n given in (31) but with n replaced by n_κ. The quantities $\Lambda_M^{(\kappa,+)}$ and $\Lambda_M^{(\kappa,-)}$ represent the inner and outer traces of $\Lambda_M(f_M^h(t))$, respectively, along the boundary of the element κ. We assume $\Lambda_M^{(\kappa,-)} = \Lambda_M^h(f_{in})$ for elements with $\partial\kappa \cap \partial\Omega_h \neq \emptyset$.

Proof. See appendix E. □

Along with being stable, it is intuitive to prescribe boundary conditions through an upwind kinetic numerical flux. For this reason, earlier works have proposed such a boundary treatment for non-linear moment equations [1, 22]. Below we consider the variational form (given in (40)) in a spatially continuous setting, and by showing that it prescribes incorrect number of boundary conditions, we show that it is ill-posed.

Remark 6. *To recover a DG discretization from (43), we can expand the approximation space $V_{h,M}$ by including functions that are discontinuous along all the element's boundaries. Such a DG discretization differs from a CG discretization (given in (40)) only in terms of inter-element fluxes. The following analysis assumes a continuously differentiable solution for which the inter-element fluxes vanish, making a DG discretization the same as the CG one. Therefore, our analysis is also valid for a DG discretization.*

Discussion: From the proof of the above result (see appendix E), we know that on a spatially continuous level the variational form in (40) is equivalent to the following.

$$\begin{aligned}
&\text{Find } \Lambda_M(f_M(t)) \in \left[H^1(\Omega)\right]^{\Xi^M} \text{ such that} \\
&\int_\Omega \phi^{\mathrm{T}} \partial_t \Lambda_M(f_M(t))dx + \sum_{i=1}^d \int_\Omega \phi^{\mathrm{T}} A_M^{(i)} \partial_{x_i} \Lambda_M(f_M(t))dx - \int_\Omega \phi^{\mathrm{T}} P_M \Lambda_M(f_M(t))dx \\
&\qquad = \frac{1}{2} \oint_{\partial\Omega} \phi^{\mathrm{T}} \left(A_M^n - D_M^n\right) \left(\Lambda_M(f_M(t)) - \Lambda_M(f_{in}(t))\right) ds, \ \forall\, \phi \in \left[H^1(\Omega)\right]^{\Xi^M}, \ \forall\, t \in [0,T].
\end{aligned} \tag{44}$$

Above, $\left[H^1(\Omega)\right]^{\Xi^M}$ denotes a standard Sobolev space of vector valued functions that is also the limit space of V_h for $h \to 0$. For brevity, we have suppressed the initial conditions.

We restrict to those solutions of the variational problem (44) that are continuously differentiable in space and time. Such a solution satisfies the moment system

$$\partial_t \Lambda_M(f_M(x,t,\cdot)) + \sum_{i=1}^d A_M^{(i)} \partial_{x_i} \Lambda_M(f_M(x,t,\cdot)) = P_M \Lambda_M(f_M(x,t,\cdot)). \tag{45}$$

Moreover, to make the boundary integral in (44) vanish, such a solution should satisfy

$$\left(A_M^n - D_M^n\right) \Lambda_M(f_M(x,t,\cdot)) = \left(A_M^n - D_M^n\right) \Lambda_M(f_{in}(x,t,\cdot)), \quad \forall \quad (x,t) \in \partial\Omega \times [0,T], \tag{46}$$

where A_M^n and D_M^n are given in (31) and (43), respectively.

The relation in (46) prescribes Ξ^M (i.e. the total number of moments) boundary conditions if $(A_M^n - D_M^n)$ is invertible. Invertibility of $(A_M^n - D_M^n)$ follows from the following argument. By definition, A_M^n and D_M^n are symmetric implying that $(A_M^n - D_M^n)$ is symmetric. Moreover, $(A_M^n - D_M^n)$ is negative definite because for all $r \in K$ $(r \neq 0)$ we have

$$\begin{aligned}
\left(\Lambda_M(r)\right)^{\mathrm{T}} \left(A_M^n - D_M^n\right) \Lambda_M(r) &= \left(\Lambda_M(r)\right)^{\mathrm{T}} \left(\int_{\xi_i n_i < 0} \Psi_M \xi_i n_i \left(\Psi_M\right)^{\mathrm{T}} f_0 d\xi \right) \Lambda_M(r) \\
&= \int_{\xi_i n_i < 0} \left(\Lambda_M(r) \cdot \Psi_M f_0\right)^2 \xi_i n_i f_0^{-1} d\xi < 0.
\end{aligned}$$

Symmetricity and negative definiteness of $(A_M^n - D_M^n)$ implies that it is invertible.

Hence, the relation in (46) prescribes Ξ^M boundary conditions. The total number of incoming characteristics for the linear moment system (45) are equal to the total number of odd moments i.e., Ξ_o^M. Since $\Xi_o^M < \Xi^M$, the relation in (46) prescribes more boundary conditions than the number of incoming characteristic implying that it is ill-posed [21].

Remark 7. *For $h > 0$, the variational form (40) has a viscous term along the boundary that allows for more boundary terms than those needed by the moment system (26a). However, for $h \to 0$ the viscosity vanishes and the same must hold for the extra boundary terms. As discussed above, this is certainly not the case for the variational form in (26a). For a small enough viscosity (that results from a small enough grid size), the non-vanishing boundary terms could result in a steep boundary layer that can cause oscillations in both the CG and the higher-order DG schemes. In the coming section, we observe such oscillations that could be a result of these steep boundary layers. First-order finite volume schemes do not show such oscillations, which could explain the absence of oscillations in the results reported in [1, 2]. A further analytical study is needed to pinpoint the exact reason behind the oscillations we report later.*

5. Numerical Results

Through numerical experiments, we study both the spatial discretization error and the physical accuracy of moment solutions computed using different penalty matrices. We define the spatial discretization error as

$$E_{\Omega_h,M} := \|f_M(\cdot,T,\cdot) - f_M^h(\cdot,T,\cdot)\|_{L^2(\Omega\times\mathbb{R}^d, f_0^{-1})}, \tag{47}$$

which is the L^2-error in approximating a given moment system using the continuous Galerkin scheme (36). We quantify the physical accuracy of a moment approximation using the following L^2-error in macroscopic quantities

$$E_{\mathcal{I},M} := \sqrt{\sum_{\alpha\in\mathcal{I}} (e_{\alpha,M})^2} \quad \text{where} \quad e_{\alpha,M} := \|\alpha_{\text{ref}}(\cdot,T) - \alpha_M(\cdot,T)\|_{L^2(\Omega)}. \tag{48}$$

Above, $\mathcal{I}$ is a set containing the macroscopic quantities defined in (20). These quantities are linear combinations of the expansion coefficients $\lambda_m(f_M^h(x,t,\cdot))$ given in (25), and one can find their explicit expressions in [7, 32, 43]. The quantity α_{ref} refers to a macroscopic quantity computed using a reference solution, the details of the reference solutions are given later.

To study the physical accuracy of moment approximations, we compute $E_{\mathcal{I},M}$ and study its convergence rate with M. For the test cases we consider, the exact macroscopic moments (i.e. α_M) are not known that prohibits a direct computation of $E_{\mathcal{I},M}$. Therefore, we approximate $E_{\mathcal{I},M}$ by $E_{\Omega_h,\mathcal{I},M}$ where $E_{\Omega_h,\mathcal{I},M}$ is the same as $E_{\mathcal{I},M}$ but with α_M replaced by its approximation α_M^h. The error $E_{\Omega_h,\mathcal{I},M}$ includes both the spatial discretization and the moment approximation error. To ensure that the moment approximation error dominates $E_{\Omega_h,\mathcal{I},M}$, we choose Ω_h such that the convergence rate of $E_{\Omega_h,\mathcal{I},M}$, with respect to h, is minimal. We label such a Ω_h as $\Omega_{h_{\min}}$ where $h_{\min}$ signifies the minimum grid-size for which the spatial discretization error dominates $E_{\Omega_h,\mathcal{I},M}$. In algorithm 1, we provide a pseudo-code for computing $\Omega_{h_{\min}}$. The algorithm terminates as soon as the convergence rate of $E_{\Omega_h,\mathcal{I},M}$, between two subsequent refinements of Ω_h, falls below a positive user-defined tolerance TOL. In the coming discussion, a reference to $E_{\mathcal{I},M}$ will mean its approximation through $E_{\Omega_{h_{\min}},\mathcal{I},M}$.

In all the experiments, we use a fourth-order Runge-Kutta scheme for temporal discretization, and we invert the mass matrix in the FE discretization directly. For steady-state problems, we assume that we reach steady-state when the rate of change in $\|f_M^h\|_X$ is less than 10^{-8}.

Algorithm 1 `COMPUTE_`$\Omega_{h_{\min}}$

INPUT: Ω_{h_0}, TOL, M
OUTPUT: $\Omega_{h_{\min}}$

$l \leftarrow 0$
$E_l \leftarrow E_{\Omega_{h_l},\mathcal{I},M}$
rate $\leftarrow \infty$
while rate $>$ TOL **do**
  $E_l \leftarrow E_{\Omega_{h_l},\mathcal{I},M}$
  $\Omega_{h_{l+1}} \leftarrow$ `refine_grid`(Ω_{h_l})
  $E_{l+1} \leftarrow E_{\Omega_{l+1},\mathcal{I},M}$
  rate $\leftarrow \log\left(E_{l+1}/E_l\right)/\log\left(h_l/h_{l+1}\right)$
  $l \leftarrow l+1$
end while
$\Omega_{h_{\min}} \leftarrow \Omega_l$

5.1 Physical Accuracy Comparison For the following test cases, we consider a square domain $\Omega = (0,1)\times(0,1)$ with all the four boundaries being fully accommodated solid walls. The details of an accommodation model are given in subsection 3.4. We fix the Knudsen number to 0.1, and we consider a linearised BGK collision model. The test case dependent initial data and the values of the boundary parameters (v^{in} and θ^{in}) are as follows.

(i) **Gaussian density in a box (Test-1):** As the initial data we consider

$$f_I(x,\xi) = \frac{\rho_I(x)}{\sqrt[3]{2\pi}}\exp\left(-\frac{\xi_i\xi_i}{2}\right), \quad \rho_I(x) = \prod_{i=1}^{2}\exp\left(-50\times\left(x_i-\frac{1}{2}\right)^2\right).$$

Velocity and temperature deviations (i.e. v^{in} and θ^{in}) for all the walls are zero, and the final time is $T = 0.3$.

(ii) **Oscillating lid-driven cavity flow (Test-2):** We consider zero initial data, $f_I = 0$. As boundary data, we consider a harmonic tangential velocity for the top wall

$$v_2^{in}(x_1, x_2 = 1, t) = \sin(4\pi t), \quad \forall \quad (x_1,t)\in(0,1)\times[0,T].$$

Velocity (v^{in}) and temperature (θ^{in}) deviations for all the other walls are zero. As the final time we consider $T = 1$.

(iii) **Lid-driven cavity flow (Test-3):** This test case is the same as the previous one, but rather than an oscillating tangential wall velocity, we consider a constant tangential wall velocity

$$v_2^{in}(x_1, x_2 = 1, t) = 1, \quad \forall \quad (x_1,t)\in(0,1)\times[0,T].$$

We look for a steady-state solution.

(iv) **Heated cavity (Test-4):** We consider zero initial data $f_I = 0$, and we heat the bottom wall with a constant temperature

$$\theta^{in}(x_1, x_2 = 0, t) = 1, \quad \forall \quad (x_1,t)\in(0,1)\times[0,T].$$

We consider zero velocity (v^{in}) and temperature (θ^{in}) deviations for all the other walls, and we look for a steady state solution.

Reference solution: We use a discrete velocity method (DVM) to compute our reference solution. For two-dimensional problems, we make the DVM efficient by projecting the BE along the ξ_3 velocity direction. In appendix F we present the equations resulting from this projection, further details can be found in [38]. For spatial discretization, we use the continuous Galerkin method given in (36) where we discretize Ω with $N_x^{\text{dvm}} \times N_x^{\text{dvm}}$ uniform elements. As discrete velocity points, we consider a set of tensorised $N \times N$ Gauss-Legendre quadrature points on each of the four quadrants $[0, c] \times [0, c]$, $[0, c] \times [-c, 0]$, $[-c, 0] \times [0, c]$ and $[-c, 0] \times [-c, 0]$, where $c \in \mathbb{R}^+$ is the velocity cut-off. A separate tensorised grid for each velocity quadrant allows for an accurate treatment of the BE's boundary conditions.

For the non-liner BE, authors in [3] provide an approximation for the velocity cut-off c. We assume that their approximation is valid also for the linearised BE resulting in

$$c \approx \max_{x \in \Omega, t \in [0,T]} \left(\hat{u}(x,t) + 4\sqrt{|\theta(x,t)|} \right),$$

where $\hat{u}(x,t) = \max\{|u_1(x,t)|, |u_2(x,t)|\}$. We estimate $\hat{u}$ and θ by u^{in} and θ^{in}, respectively, and we take a maximum over all the test cases, this provides $c = 1 + 4\sqrt{1} = 5$. Note that we need the modulus over θ because it is the temperature deviation (20), which could be negative. We start with $(N_x^{\text{dvm}}, N) = (10, 5)$, and keep on increasing N_x^{dvm} by 15 and N by 5 until the relative L^2-error in all macroscopic quantities between two subsequent increments falls below a tolerance of 10^{-3}. For the Gaussian density in a box test case, the relative L^2-error in different macroscopic quantities, under subsequent refinement of the DVM, is shown in Figure 1. We reach the desired tolerance for $N = 20$ and $N_x^{\text{dvm}} = 100$. Results for other test cases are similar and are not shown for brevity. Once we have the above values of N and N_x^{dvm}, for assurance we increase c by one and re-compute all the macroscopic quantities. For all the test cases, the re-computed macroscopic quantities did not differ (in the L^2-sense) from the old ones by more than the machine precision implying that $c = 5$ is sufficient.

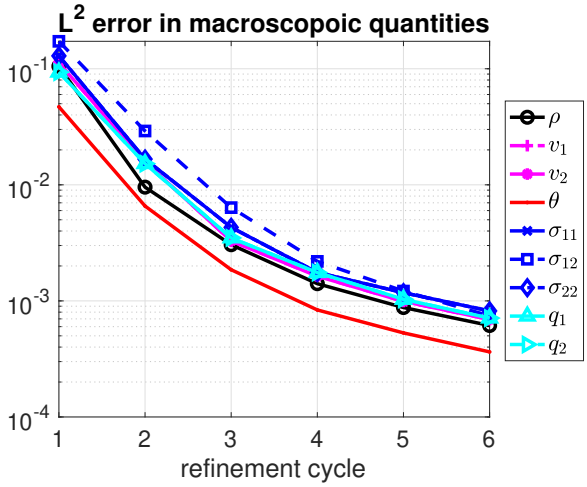

Figure 1: L^2-error in different macroscopic quantities under subsequent refinement of the DVM. Results for the Gaussian density in a box test-case.

Discretization details: We discretize Ω with $N_x \times N_x$ uniform elements and use the same value of N_x for all the test cases, we vary M over the set $\{3, \ldots, 13\}$. To find N_x, we use the routine `COMPUTE_`$\Omega_{h_{\min}}$. The purpose of `COMPUTE_`$\Omega_{h_{\min}}$ is to find a spatial grid for which the moment approximation error dominates $E_{\Omega_h, I, M}$. Since the moment approximation error is minimal for either $M = 12$ or $M = 13$ (a moment approximation might have oscillatory convergence), it is sufficient to run `COMPUTE_`$\Omega_{h_{\min}}$ for $M = 12$ and $M = 13$.

As Ω_{h_0}, which is the input to COMPUTE_$\Omega_{h_{\min}}$, we choose a grid with 10×10 elements, and during `refine_grid` we increase the number of elements in each direction by five. We choose TOL $= 10^{-1}$. Figure 2 shows the convergence rate of $E_{\Omega_h,\mathcal{I},M}$ after every refinement cycle inside the algorithm COMPUTE_$\Omega_{h_{\min}}$. The refinement cycle here refers to the index l inside the algorithm. Results are shown for $M = 12$ and are computed with a characteristic penalty matrix. Results for $M = 13$ and an odd penalty matrix are similar. The reason for not including the kinetic penalty matrix will be clear later. Table 1 shows the value of N_x resulting from COMPUTE_$\Omega_{h_{\min}}$. To maintain consistency with the DVM, we choose $N_x = 100$ for all the test cases, which is greater than all the values given in Table 1.

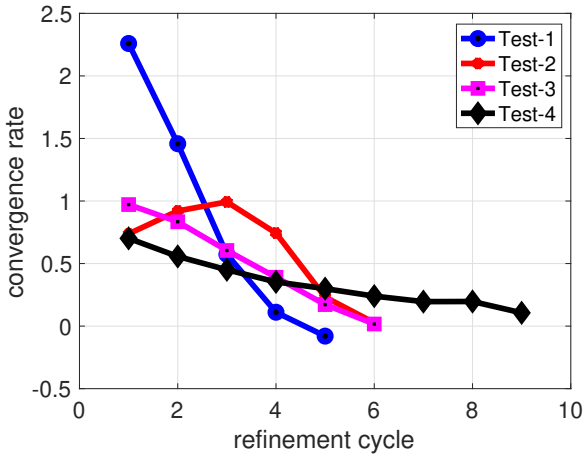

Figure 2: Convergence rate after every refinement cycle inside COMPUTE_$\Omega_{h_{\min}}$. Computations done using $M = 12$ and a characteristic penalty matrix.

Test case	Test-1	Test-2	Test-3	Test-4
N_x	35	40	40	55

Table 1: Result from COMPUTE_$\Omega_{h_{\min}}$.

Remark 8. *In all the coming numerical experiments, $E_{\Omega_h,\mathcal{I},M}$ converges with a rate close to one with respect to M. This rate is ten times higher than the tolerance used for the convergence rate in COMPUTE_$\Omega_{h_{\min}}$, which further justifies our choice of the tolerance.*

Comments on convergence rates: In the following test cases, we study the convergence rate of $E_{\mathcal{I},M}$ with respect to M. Theoretical results against which we can validate our observed convergence rates are currently non-existent. Although the authors in [30, 31] perform an a-priori convergence analysis, they focus on a half-space spatial domain (i.e. $\Omega = (-\infty, 0) \times (-\infty, \infty) \times \ldots \times (-\infty, \infty)$) that is not of much practical relevance. As compared to a half-space domain, a square domain has an irregular boundary, making it difficult to extend the convergence analysis.

Despite the lack of a theoretical underpinning, the convergence rates for $E_{\mathcal{I},M}$ we present here have the following similarities to those presented for half-space problems [43]. Firstly, the convergence rate is test-case dependent. Secondly, the convergence rate might oscillate for even and odd values of M. These oscillations are the most prominent for steady-state problems; see for example the heated cavity test case 10(b). Thirdly, in all the test cases, the convergence rate stays approximately between 1 and 1.5. The first similarity results from a moment approximation being a Galerkin method for which the convergence rate is solution's regularity dependent, and that is in turn test case dependent. A possible explanation for the

second observation (motivated from the error bound for half-space problems [31]) is that the terms in a moment approximation's error bound, which degrade the convergence rate, vanish for even or odd values of M, thus leading to oscillations. However, even for half-space problems, a definitive explanation is missing, and a further analytical investigation is needed. The third similarity shows that for square domains, a moment approximation retains a similar accuracy as for a half-space domain, indicating that an error bound similar to a half-space problem must be feasible for a square (or more general) domain.

In addition to oscillations in $E_{\mathcal{I},M}$, we also observe oscillatory convergence for L^2-errors in different macroscopic quantities. However, for a given test case, not all macroscopic quantities show oscillations in their error values. For example, in the oscillating lid-driven cavity flow (fig-6(c)), the error in v_1 does not oscillate whereas the error in v_2 does. Moreover, the error in a particular macroscopic quantities does not need to oscillate for every test case. For example, the error in ρ oscillates for the heated cavity test case (fig-10(c)) but does not oscillate for the Gaussian density in a box (fig-3(c)) test case. This test case dependent convergence of the L^2-error in macroscopic quantities also results from the test-case dependent solution's regularity.

Gaussian density in a box (Test-1): Fig-3(b) shows the similarity in $E_{\mathcal{I},M}$ computed using the characteristic and the odd penalty matrices. For both the penalty matrices, $E_{\mathcal{I},M}$ converges monotonically with a rate close to 1.5. However, the error in individual macroscopic quantities $e_{\alpha,M}$ does not necessarily converge monotonically; see fig-3(c) and fig-3(d). As an example consider σ_{12} that converges monotonically with M whereas σ_{11} does not. Fig-4(a) and fig-4(b) shows that for odd and even values of M, convergence rates of $e_{\alpha,M}$ differ very slightly. This difference will be substantial in the following test cases.

To study the solution computed using a kinetic penalty matrix, we simultaneously increase the value of M and the value of N_x. We consider five refinement cycles with (M, N_x) being $(3, 60)$, $(4, 80)$, $(5, 100)$, $(6, 120)$ and $(7, 140)$. Fig-5(a) shows the deviation in density along a cross-section resulting from these five refinement cycles. For all the refinement cycles, the solution oscillates close to the boundary. As the final time is increased from $T = 0.3$ to $T = 0.6$, the oscillations reach the interior of the domain and pollute the entire solution. Fig-5(c) shows such a solution for $M = 5$, similar results were observed for other values of M. These oscillations are absent in solutions computed using the characteristic penalty matrix (see fig-5(b)). Since the FE approximation is stable (see lemma 4.1), despite the oscillations, the solution does not blow up in time. A possible explanation for these oscillations could be the one given in remark 7.

Proving convergence (or non-convergence) numerically is impossible because one cannot let $M, N_x \to \infty$. However, the oscillations do not vanish under the limited number of refinements considered above indicating that the sequence of moment solutions computed using the kinetic penalty matrix does not seem to convergence to the BE's solution.

Remark 9. *Since the use of a weak kinetic boundary discretization leads to oscillatory solutions for all the following test cases, we refrain from discussing its results further. For the same reason, we do not use weak kinetic boundary discretization for discretization error comparison.*

Oscillating lid-driven cavity flow (Test-2): Only for even values of M, $E_{\mathcal{I},M}$ differs (see fig-6(b)) for the characteristic and the odd penalty matrix. Moreover, only for a characteristic penalty matrix $E_{\mathcal{I},M}$ shows oscillatory convergence. Convergence rate of $E_{\mathcal{I},M}$ stays close to one for both the penalty matrices. In comparison to the previous test case, there is a significant difference in the convergence rates of $e_{\alpha,M}$ for the odd and even values of M; see 7(a) and 7(b).

Lid-driven cavity flow (Test-3): Like the previous test case, values of $E_{\mathcal{I},M}$ computed with a characteristic and an odd penalty matrix differ only for even values of M; see fig-8(b). Increasing

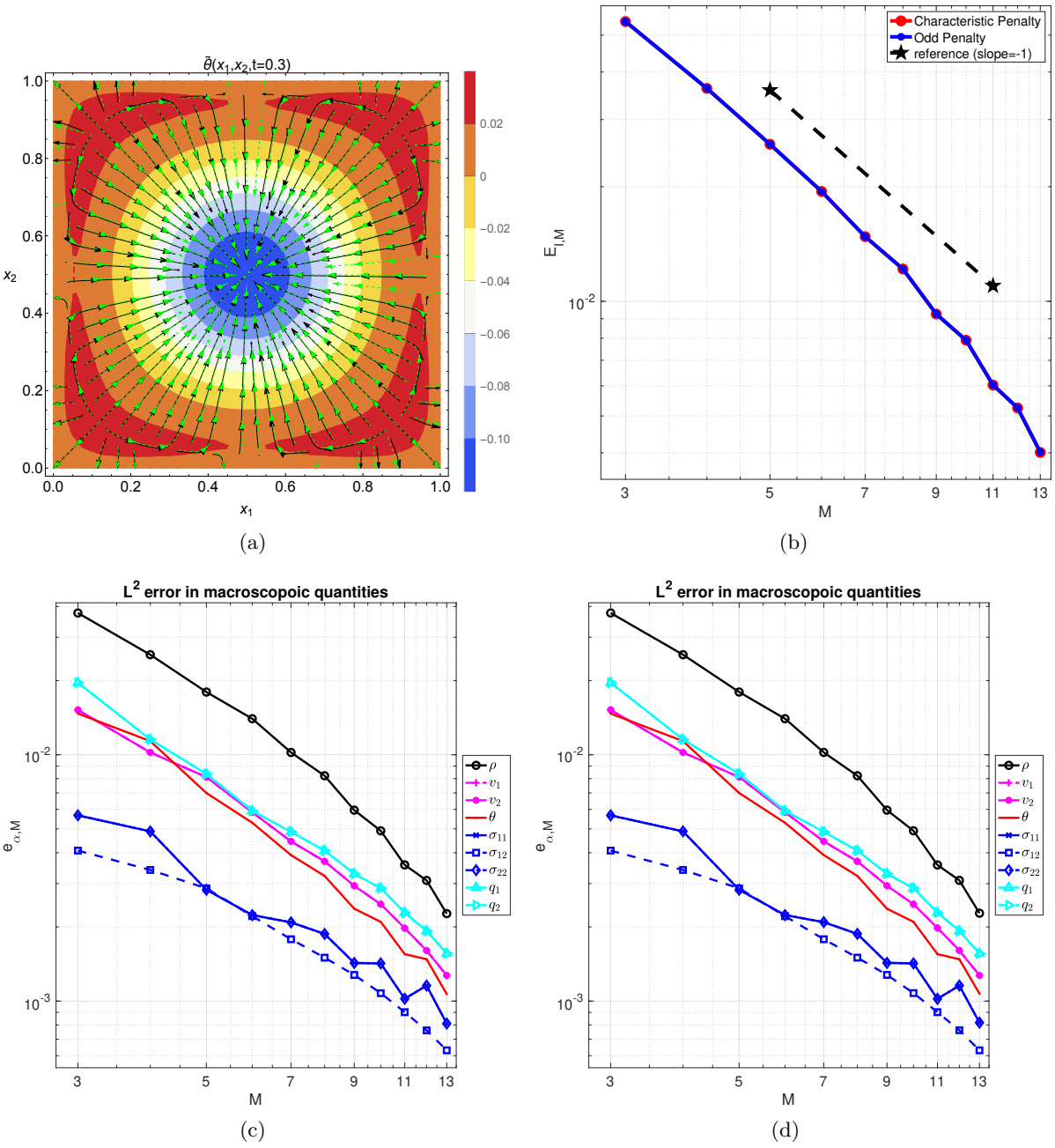

Figure 3: Results for the Gaussian density in a box test case. (a) θ contours computed with $M = 13$, at $t = 0.3$, over-plotted with heat flux streamlines computed with DVM (green) and $M = 13$ (black). (b) Comparison of $E_{\mathcal{I},M}$ computed with a characteristic and an odd penalty matrix. $e_{\alpha,M}$ computed with a characteristic (c) and an odd (d) penalty matrix.

the value of M leads to oscillations in $E_{\mathcal{I},M}$ for both the penalty matrices, this is in contrast to the previous test case where $E_{\mathcal{I},M}$ showed oscillations for only the characteristic penalty matrix. Only for even values of M, we observe a significant difference in convergence rates of $e_{\alpha,M}$; see fig-9(a) and fig-9(a).

Heated cavity (Test-4): For both the odd and the characersitic penalty matrix, $E_{\mathcal{I},M}$ oscillates and shows faster convergence for odd values of M; see fig-10(b). Moreover, only for

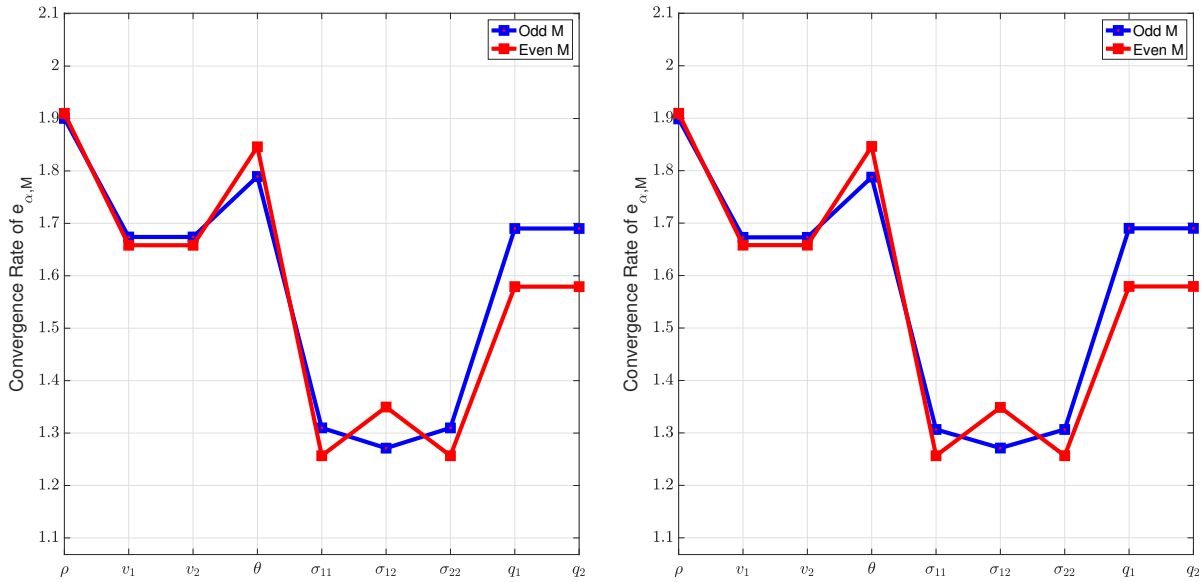

(a) (b)

Figure 4: Results for the Gaussian density in a box test case. Convergence rate of $e_{\alpha,M}$ computed with (a) characteristic penalty matrix, and (b) odd penalty matrix.

odd values of M, $E_{\mathcal{I},M}$ differs between the two penalty matrices. For the convergence rates of the error $e_{\alpha,M}$, we observe the following. With a characteristic penalty matrix (fig-11(a)), odd values of M provide a higher convergence rate for all the macroscopic quantities. Whereas with an odd penalty matrix (fig-11(b)), neither the odd nor the even values of M provide a higher convergence rate for all the macroscopic quantities.

Rarefaction effects: In the lid-driven cavity flow, moving the top wall tangentially creates a hot and a cold region near the upper right and the upper left corner of the domain, respectively. See fig-8(a) for the temperature profile in a lid-driven cavity flow. Fourier's heat flux law dictates that near thermodynamic equilibrium, heat flows from a hot to a cold region. However, significant deviations from equilibrium can trigger an anti-Fourier heat flux that flows in the opposite direction i.e., from a cold to a hot region. The heat-flux streamlines in fig-8(a) show that the lid-driven cavity flow has an anti-Fourier heat flux which is not observed for the oscillating lid-driven cavity flow (see fig-6(a)).

For a lid-driven cavity flow, fig-12(a) shows the velocity component v_1 along the cross-section $x_1 = 0.5$. At $x_2 = 1$, gas velocity differs from that of the wall, creating the so-called velocity slip. Both the solutions computed using a characersitic penalty matrix and an odd penalty matrix capture the velocity slip accurately. Similar is the case for the heated cavity test case (see fig-12(b)) where gas temperature differs from the wall temperature, creating the so-called temperature jump. The anti-Fourier heat flux, the temperature jump, and the velocity slip are classical rarefaction effects, all of which have been reported in the previous works [9, 28, 29, 43].

Similar to rarefaction in gas, the use of a SAT might also lead to a velocity slip or a temperature jump. The rarefaction and the SAT induced boundary effects differ in the sense that the former results from gas deviating from a thermodynamic equilibrium whereas the later is a numerical artefact resulting from a finite grid size. Being models for gases close to a thermodynamic equilibrium, neither Euler nor the Navier-Stokes equations capture the rarefaction boundary effects, but for a finite grid size, the use of a SAT can induce boundary effects in both the equations [27, 40]. Moreover, as the grid size tends to zero, boundary effects induced by

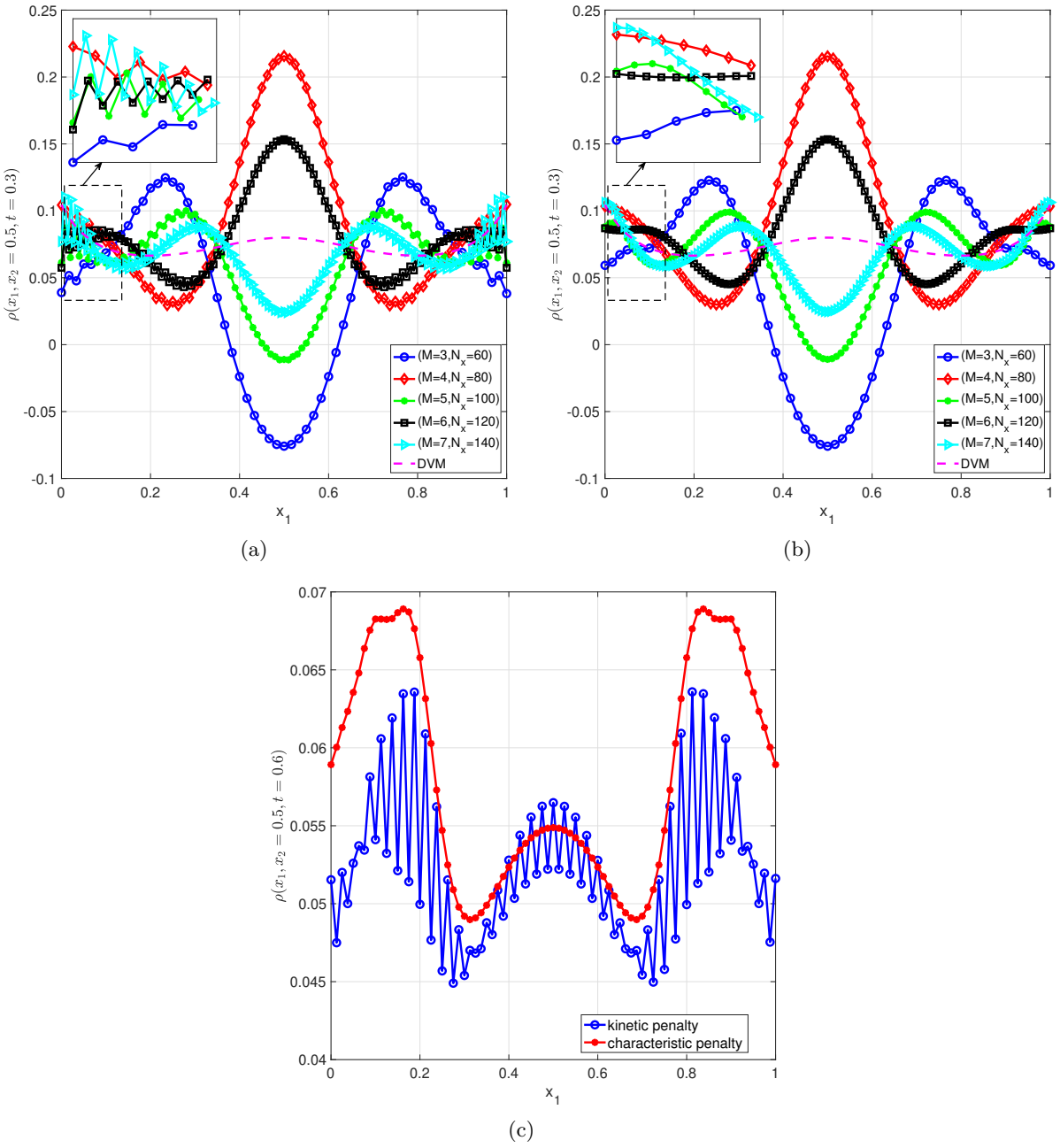

Figure 5: Results for the Gaussian density in a box test case. Deviation in density along the cross-section $x_2 = 0.5$. (a) Results for a kinetic penalty matrix, and (b) results for a characteristic penalty matrix. (c) Compares the long-time behaviour of the solutions computed using a characteristic and a kinetic penalty matrix.

rarefaction persist whereas those induced by a SAT (for a convergent numerical scheme) vanish. Note that our choice of Ω_h ensures that the spatial discretization error does not dominate, therefore the boundary effects reported in fig-12(a) and fig-12(b) are rarefaction dominated.

5.2 Discretization Error Comparision We consider a square $\Omega = (0,1) \times (0,1)$ as our spatial domain, and we discretize it with $N_x \times N_x$ uniform square elements. We choose five different values for N_x, $N_x = \{16, 32, 64, 128, 256\}$ which corresponds to the grid sizes $h = \{\frac{1}{16}, \frac{1}{32}, \frac{1}{64}, \frac{1}{128}, \frac{1}{256}\}$. We consider $M = 3$ (corresponds to the Grad's-20 moment system

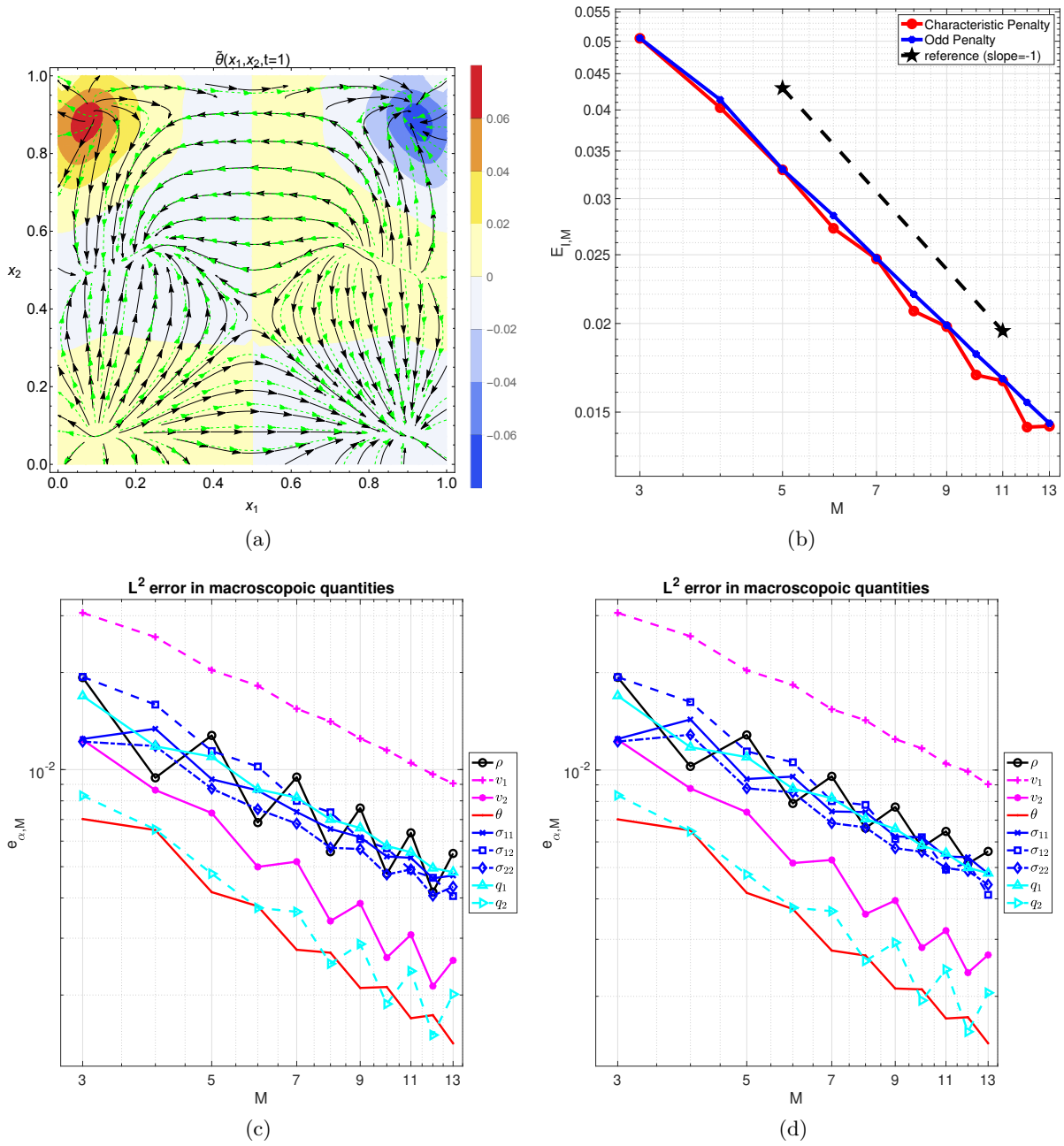

Figure 6: Results for the oscillating lid-driven cavity flow test case. (a) θ contours computed with $M = 13$, at $t = 0.3$, over-plotted with heat flux streamlines computed with DVM (green) and $M = 13$ (black). (b) Comparison of $E_{\mathcal{I},M}$ computed with a characteristic and an odd penalty matrix. $e_{\alpha,M}$ computed with a characteristic (c) and an odd (d) penalty matrix.

[8]), and use the method of manufactured solutions. As the exact solution we consider

$$(\Lambda_M(f_M(x,t,.)))_i = \begin{cases} \cos(\pi t)\sin(\pi x_1)\sin(\pi x_2), & i = 1 \\ 0, & \text{else} \end{cases} \tag{49}$$

where $\Lambda_M(f_M(x,t,.))$ is a vector containing all the expansion coefficients, and is given in definition 3.3. Note that for a 2D physical space, moment system with $M = 3$ has $\Xi^M = 13$ unknowns [43], and therefore the above index i runs from 1 to 13. To ensure that the above function is

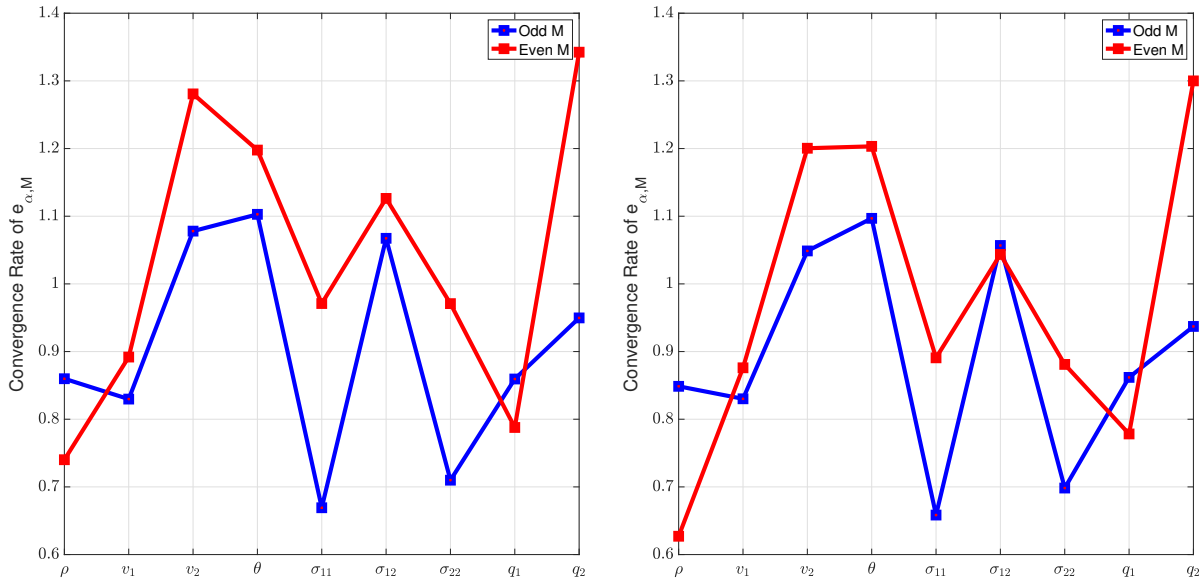

(a) (b)

Figure 7: Results for the oscillating lid-driven cavity flow test case. Convergence rate of $e_{\alpha,M}$ computed with (a) characteristic penalty matrix, and (b) odd penalty matrix.

a solution to the moment system, we add a forcing term $F(x,t)$ to the right of (26a). Explicit form of $F(x,t)$ is given as

$$(F(x,t))_i = \begin{cases} -\pi \sin(\pi t)\sin(\pi x_1)\sin(\pi x_2), & i=1 \\ -\pi \sin(\pi t)\sin(\pi x_1)\sin(\pi x_2), & i=2 \\ \pi \cos(\pi t)\sin(\pi x_1)\cos(\pi x_2), & i=3 \\ 0, & \text{else} \end{cases}. \tag{50}$$

As initial data we consider the exact solution with $t=0$. We choose $\mathcal{G}_M = 0$ that ensures that the exact solution satisfies the boundary conditions in (26c). As final time we consider $T=1$. To quantify the discretization error, we use $E_{\Omega_h,M}$ defined in (47). Since weak kinetic boundary discretization leads to oscillations, we only compare solutions computed with a characteristic and an odd penalty matrix.

In fig-13 we see that $E_{\Omega_h,M}$ computed with both the penalty matrices has a convergence rate of two with respect to the grid size, which is as expected. However, $E_{\Omega_h,M}$ (see table-2) computed with a characteristic penalty matrix has a higher value as compared to the one computed with an odd penalty matrix.

	$E_{\Omega_h,M}(\times 10^5)$				
Penalty Matrix	$N_x = 16$	$N_x = 32$	$N_x = 64$	$N_x = 128$	$N_x = 256$
Characteristic (Σ_c)	389.80	97.47	24.36	6.09	1.52
Odd (Σ_o)	224.93	55.69	13.89	3.47	0.87

Table 2: Discretization errors computed with different penalty matrices. Results computed with $M=3$.

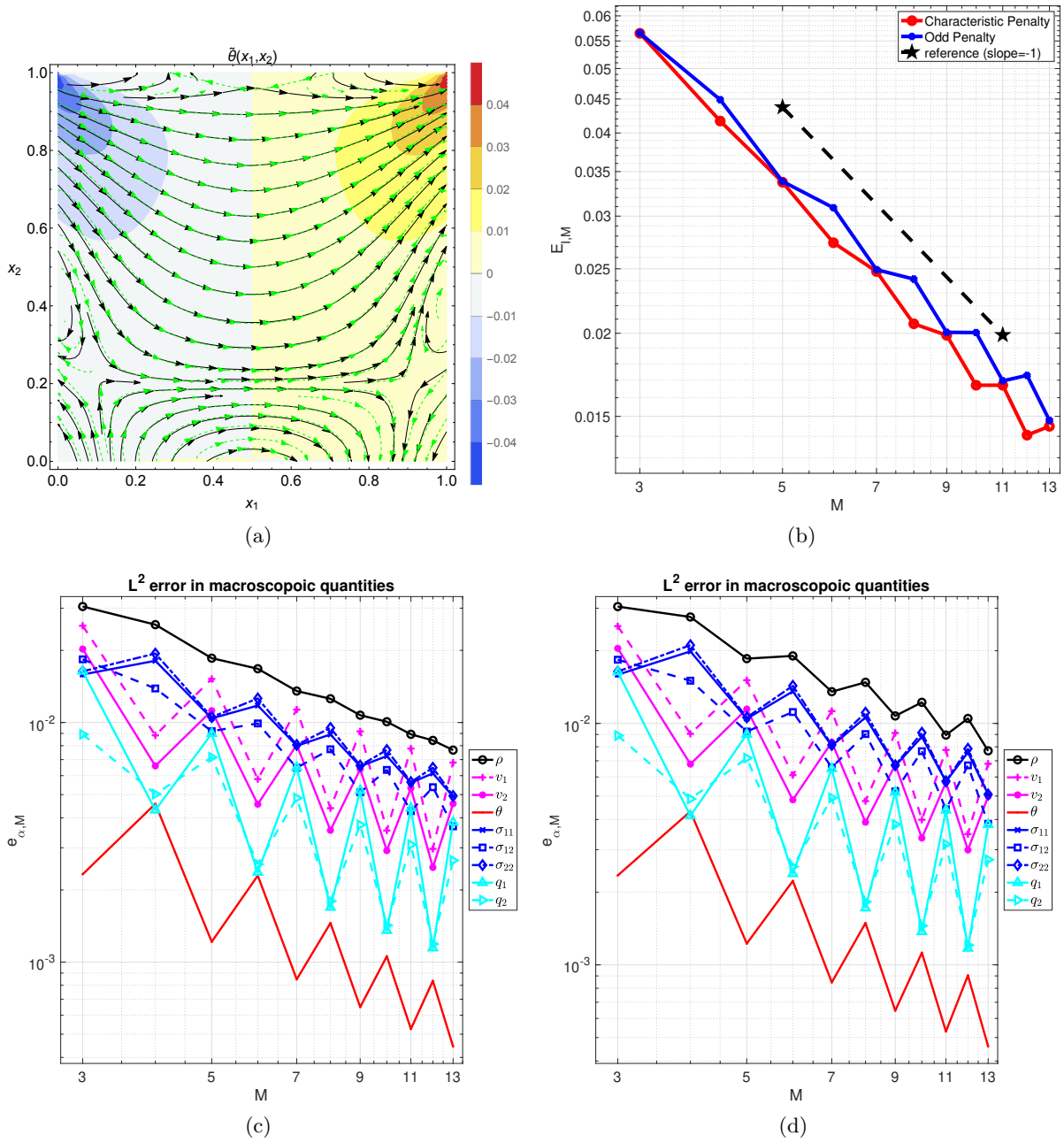

Figure 8: Results for the lid driven cavity flow test case. (a) θ contours computed with $M = 13$, at $t = 0.3$, over-plotted with heat flux streamlines computed with DVM (green) and $M = 13$ (black). (b) Comparison of $E_{\mathcal{I},M}$ computed with a characteristic and an odd penalty matrix. $e_{\alpha,M}$ computed with a characteristic (c) and an odd (d) penalty matrix.

6. Discussion and Conclusion

We presented a FE approximation that preserves the stability of linearised moment equations on a spatially discrete level. We imposed boundary conditions with a SAT term and presented three different forms of the SAT. Each of these three forms lead to a stable FE approximation, and we showed that the SAT based upon the weak kinetic boundary discretization prescribes the incorrect number of boundary conditions. Through numerical experiments, we compared the discretization error and the physical accuracy of moment solutions computed using the char-

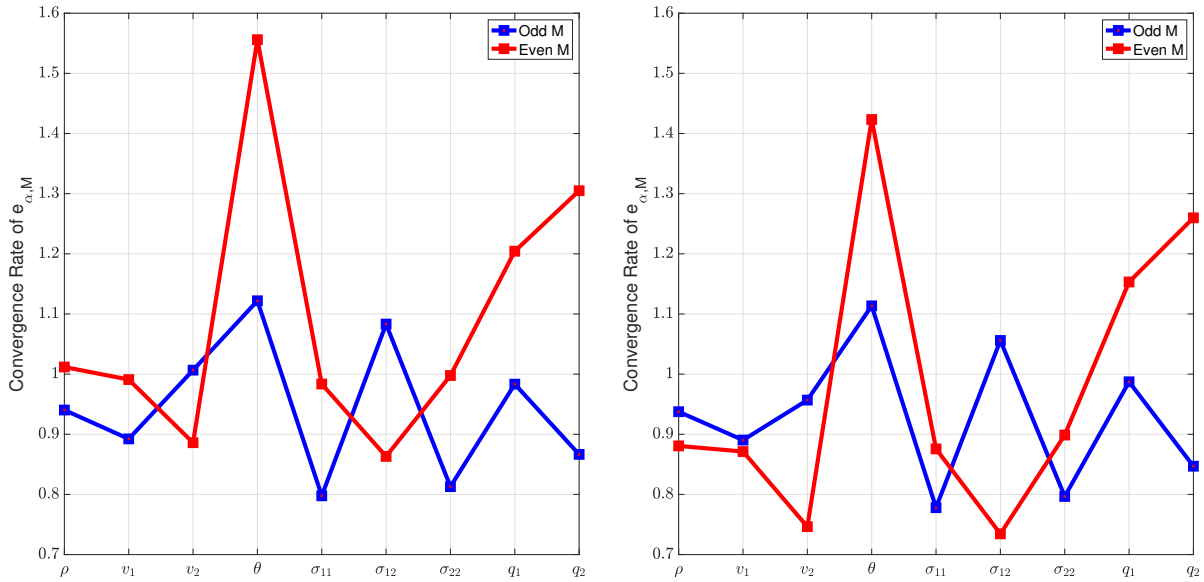

(a) (b)

Figure 9: Results for the lid-driven cavity flow test case. Convergence rate of $e_{\alpha,M}$ computed with (a) characteristic penalty matrix, and (b) odd penalty matrix.

acteristic and the odd penalty matrix. The characteristic penalty matrix was found to provide better physical accuracy, whereas the odd penalty matrix provided a lower spatial discretization error.

The use of weak kinetic boundary discretization (40) led to oscillatory solutions. Originating at the boundary, these oscillations traveled inside the domain leading to moment solutions that did not appear to converge to the DVM reference solution. Thus, at least for the linearised moment equations, weak kinetic boundary discretization fails to provide physically meaningful solutions. In [1, 22, 23, 41], authors recommend such a boundary discretization for an entropy minimisation based moment approximation. Moreover, the authors in [1] do not report oscillations in solutions to a non-linear moment approximation computed using an upwind kinetic numerical flux. This either implies that the kinetic upwinding is well-posed for non-linear moment approximations, or it could result from the use of a first order finite volume scheme that suppresses oscillations. Theoretical understanding of boundary conditions for non-linear moment systems is underdeveloped prohibiting further conclusions.

Previous studies [4, 29, 36] have (computationally) shown that by changing the matrix R_M given in (34), one can improve the accuracy of a moment approximation. Adding on to these works, our results indicate that the SAT used to discretize the boundary conditions also influences the physical accuracy. We explored only three different variants of the SAT, in future studies it might be possible to construct other variants of the SAT that will improve the accuracy of moment approximations.

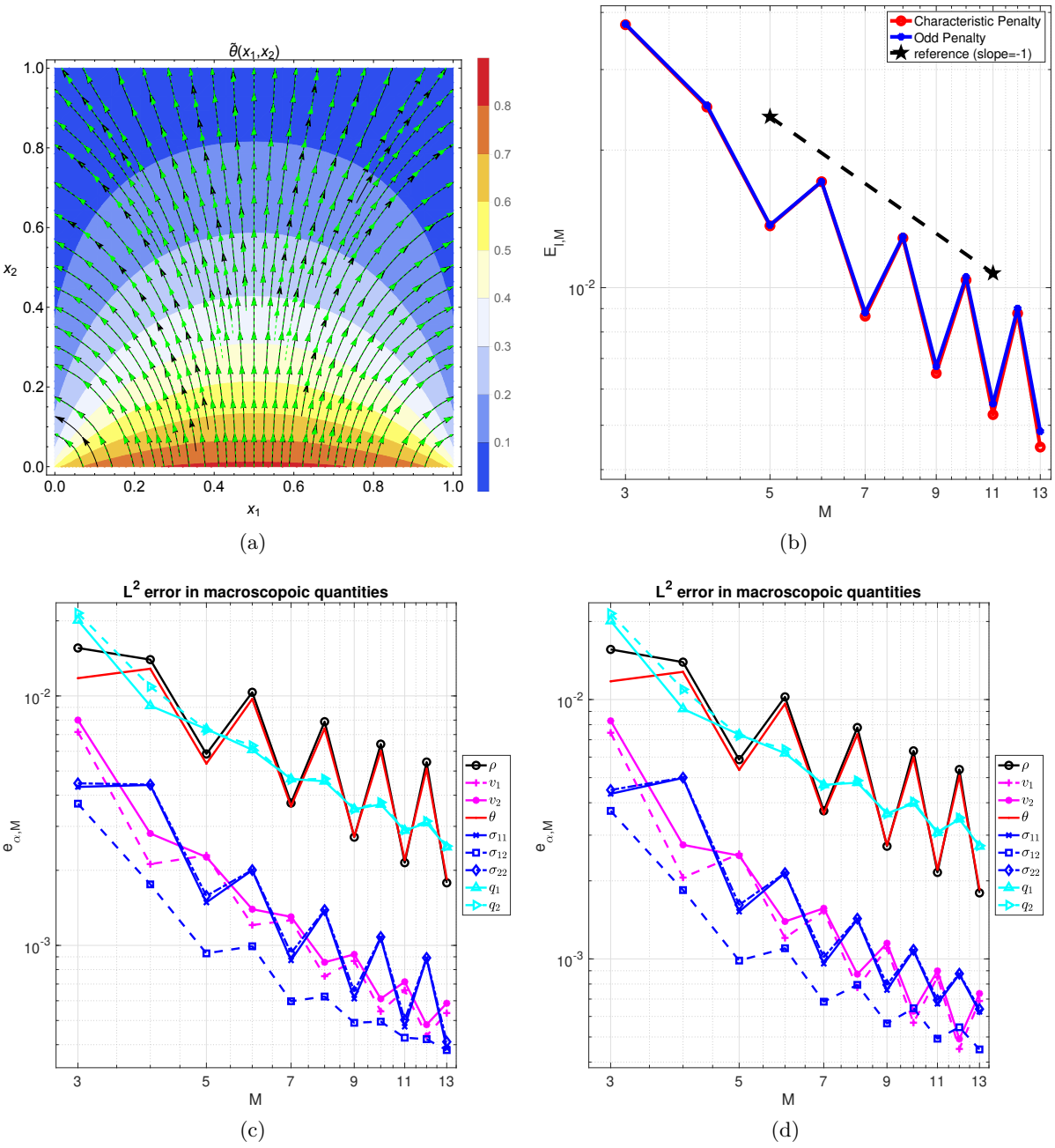

Figure 10: Results for the heated cavity test case. (a) θ contours computed with $M = 13$, at $t = 0.3$, over-plotted with heat flux streamlines computed with DVM (green) and $M = 13$ (black). (b) Comparison of $E_{\mathcal{I},M}$ computed with a characteristic and an odd penalty matrix. $e_{\alpha,M}$ computed with a characteristic (c) and an odd (d) penalty matrix.

Appendices

A. Stability with an odd penalty matrix

For convenience we define $\alpha_h^n = O^n \alpha_h$. Moreover, we assume α_n^h to be ordered as

$$\alpha_h^n = \left((\alpha_p)^{\mathrm{T}}, (\alpha_q)^{\mathrm{T}} \right)^{\mathrm{T}} \tag{51}$$

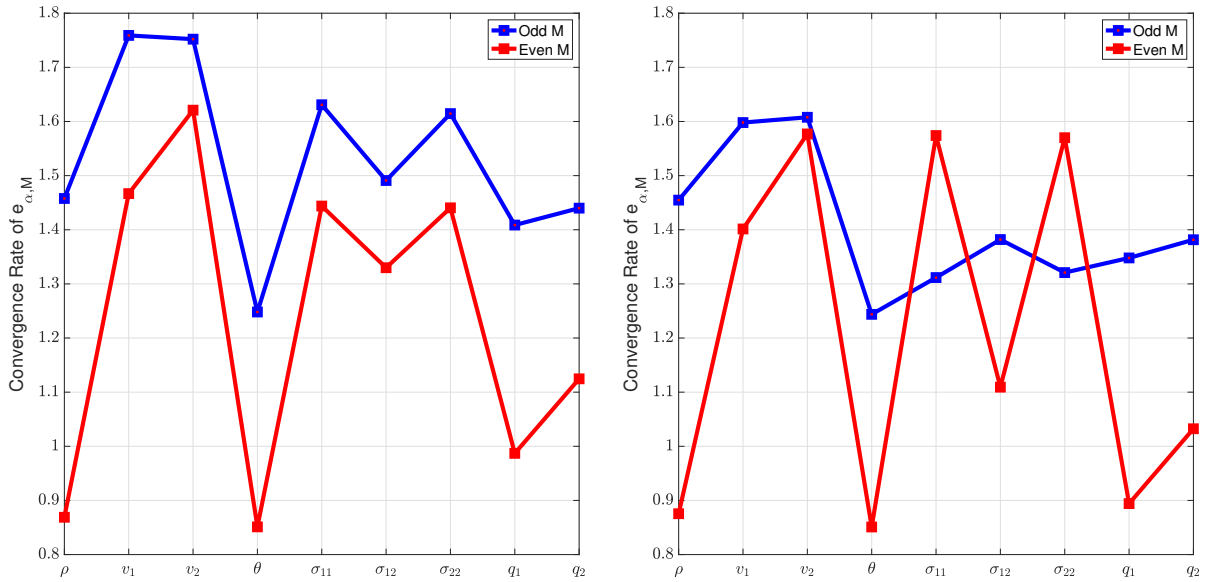

(a) (b)

Figure 11: Results for the heated cavity test case. Convergence rate, with respect to M, for $e_{\alpha,M}$ obtained with (a) characteristic penalty matrix, and (b) odd penalty matrix.

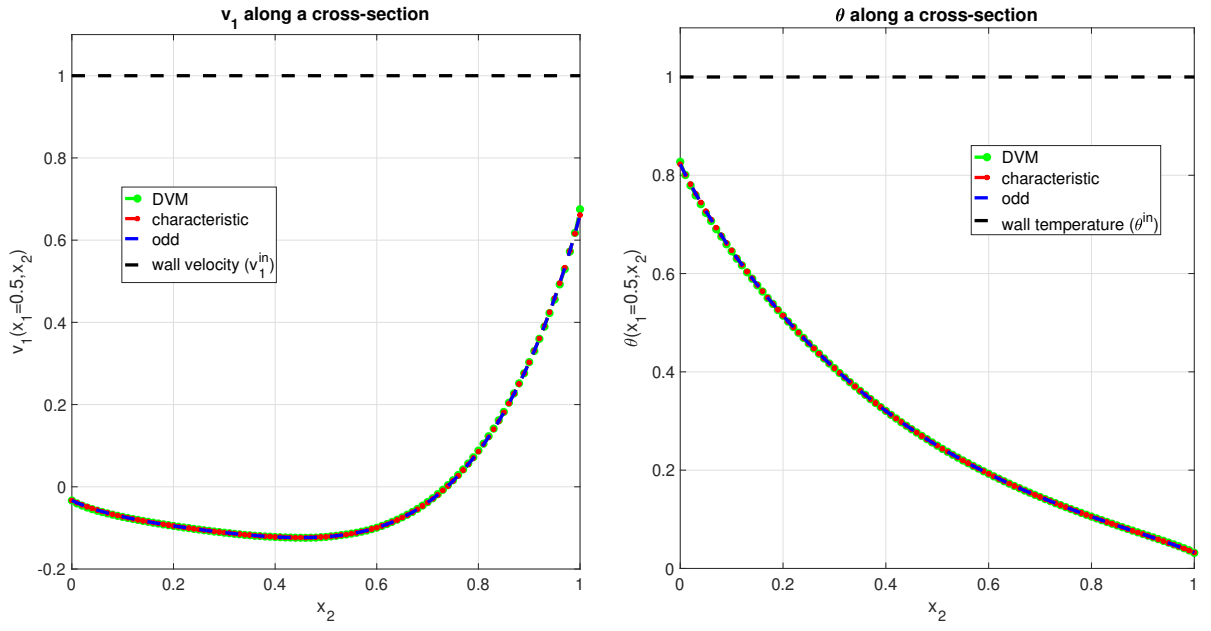

(a) (b)

Figure 12: (a) v_1 along the cross-section $x_1 = 0.5$ computed with $M = 13$ for the lid-driven cavity flow. (b) θ along the cross-section $x_1 = 0.5$ computed with $M = 13$ for the heated cavity.

with $\alpha_p \in \mathbb{R}^p$ and $\alpha_q \in \mathbb{R}^q$. To derive a stability estimate for (11) we replace Σ by Σ_o, choose ϕ as $\alpha_h(\cdot, t)$ and use the semi-negative definiteness of P to find

$$\int_{\Omega_h} (\alpha_h(t))^{\mathrm{T}} \partial_t \alpha_h(t) dx + \sum_{i=1}^{d} \int_{\Omega_h} (\alpha_h(t))^{\mathrm{T}} A^{(i)} \partial_{x_i} \alpha_h(t) dx \leq \oint_{\partial\Omega_h} \left(\tilde{A}\alpha_q(t)\right)^{\mathrm{T}} \left(B\alpha_h(t) - \mathcal{G}(t)\right) ds. \tag{52}$$

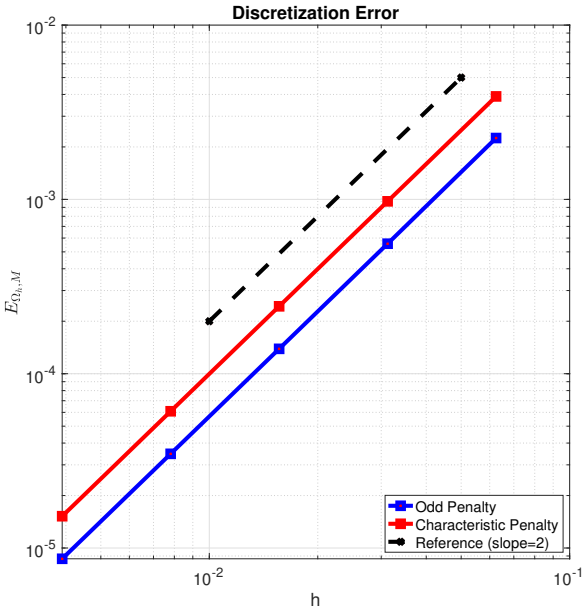

Figure 13: Comparison of discretization error. Computations done with $M = 3$.

Using the assumed structure of $A^{(1)}$ in (3) and the rotational invariance of A^n (6), we simplify the term with spatial derivatives to find

$$\begin{aligned}\sum_{i=1}^{d}\int_{\Omega_h}\left(\alpha_h(t)\right)^{\mathrm{T}}A^{(i)}\partial_{x_i}\alpha_h(t)dx =&\frac{1}{2}\oint_{\partial\Omega_h}\left(\alpha_h(t)\right)^{\mathrm{T}}A^{n}\alpha_h(t)ds\\ =&\frac{1}{2}\oint_{\partial\Omega_h}\left(O^n\alpha_h(t)\right)^{\mathrm{T}}A^{(1)}\left(O^n\alpha_h(t)\right)ds\\ =&\oint_{\partial\Omega_h}\left(\alpha_p(t)\right)^{\mathrm{T}}\tilde{A}\alpha_q(t)ds\end{aligned}\tag{53}$$

Using the above expression and the explicit form of B from (8) in (52), we find

$$\begin{aligned}\frac{1}{2}\partial_t\|\alpha_h(t)\|^2_{L^2(\Omega_h;\mathbb{R}^n)}+&\oint_{\partial\Omega_h}\left(\alpha_p(t)\right)^{\mathrm{T}}\tilde{A}\alpha_q(t)ds\\ \leq&\oint_{\partial\Omega_h}\left(\tilde{A}\alpha_q(t)\right)^{\mathrm{T}}\left(\alpha_p(t)-R\tilde{A}\alpha_q(t)-\mathcal{G}(t)\right)ds.\end{aligned}\tag{54}$$

where the assumption in assumption 3 allowed us to use chain rule for the first term on the left. Simplifying the above inequality by cancelling out common terms, we find

$$\begin{aligned}\frac{1}{2}\partial_t\|\alpha_h(t)\|^2_{L^2(\Omega_h;\mathbb{R}^n)}\leq&-\oint_{\partial\Omega_h}\left(\tilde{A}\alpha_q(t)\right)^{\mathrm{T}}\left(R\tilde{A}\alpha_q(t)+\mathcal{G}(t)\right)ds\\ \leq&\frac{1}{4}\oint_{\partial\Omega_h}\left(\mathcal{G}(t)\right)^{\mathrm{T}}R^{-1}\mathcal{G}(t)ds.\end{aligned}\tag{55}$$

For the last inequality, we have used a relation which holds true $\forall y, b \in \mathbb{R}^p$

$$y^{\mathrm{T}}Ry + y^{\mathrm{T}}b = (y-\tilde{y})^{\mathrm{T}}R(y-\tilde{y}) - \tilde{y}^{\mathrm{T}}R\tilde{y} \leq -\tilde{y}^{\mathrm{T}}R\tilde{y}, \quad \tilde{y} = -\frac{1}{2}\left(R\right)^{-1}b.$$

Due to our assumption (assumption 1) $\oint_{\partial\Omega_h}\mathcal{G}^{\mathrm{T}}R^{-1}\mathcal{G}ds \in L^\infty([0,T])$, and therefore integrating (55) over $[0,T]$ completes our proof.

B. P_3 equations of radiation transport

For simplicity, we consider a two dimensional physical space, $\Omega \subseteq \mathbb{R}^2$. We get the P_N equations of radiation transport by expanding the distribution function in terms of spherical harmonics [6]. Let Y_l^m represent a spherical harmonic where $l \in \mathbb{N}$ and $m = -l, \ldots, 0, \ldots, l$. For P_3, l varies from zero to three. Let α_l^m represent the expansion coefficients of these spherical harmonics. We assume the solution vector ($\alpha(x,t) \in \mathbb{R}^{10}$) to be ordered as

$$\alpha = \left(\alpha_1^1, \alpha_2^{-2}, \alpha_3^1, \alpha_3^3, \alpha_0^0, \alpha_1^{-1}, \alpha_2^0, \alpha_2^2, \alpha_3^{-3}, \alpha_3^{-1}\right)^{\mathrm{T}}$$

Note that all the other values of α_l^m that are not mentioned above are zero due to our assumption of a two dimensional physical space [34]. Under the assumed order for α, the flux matrices are given as

$$A^{(1)} = \begin{pmatrix} 0_{4\times4} & \tilde{A} \\ \left(\tilde{A}\right)^{\mathrm{T}} & 0_{6\times6} \end{pmatrix}$$

where

$$\tilde{A} = \begin{pmatrix} \frac{1}{\sqrt{3}} & 0 & -\frac{1}{\sqrt{15}} & \frac{1}{\sqrt{5}} & 0 & 0 \\ 0 & \frac{1}{\sqrt{5}} & 0 & 0 & \sqrt{\frac{3}{14}} & -\frac{1}{\sqrt{70}} \\ 0 & 0 & \sqrt{\frac{6}{35}} & -\frac{1}{\sqrt{70}} & 0 & 0 \\ 0 & 0 & 0 & \sqrt{\frac{3}{14}} & 0 & 0 \end{pmatrix}$$

From the explicit form of $\tilde{A}$ given above it follows that $\mathrm{rank}(\tilde{A}) = 4$. The Jacobian matrix along x_2 is given as

$$A^{(2)} = \begin{pmatrix} 0 & \frac{1}{\sqrt{5}} & 0 & 0 & 0 & 0 & 0 & 0 & 0 & 0 \\ \frac{1}{\sqrt{5}} & 0 & -\frac{1}{\sqrt{70}} & -\sqrt{\frac{3}{14}} & 0 & 0 & 0 & 0 & 0 & 0 \\ 0 & -\frac{1}{\sqrt{70}} & 0 & 0 & 0 & 0 & 0 & 0 & 0 & 0 \\ 0 & -\sqrt{\frac{3}{14}} & 0 & 0 & 0 & 0 & 0 & 0 & 0 & 0 \\ 0 & 0 & 0 & 0 & 0 & \frac{1}{\sqrt{3}} & 0 & 0 & 0 & 0 \\ 0 & 0 & 0 & 0 & \frac{1}{\sqrt{3}} & 0 & -\frac{1}{\sqrt{15}} & -\frac{1}{\sqrt{5}} & 0 & 0 \\ 0 & 0 & 0 & 0 & 0 & -\frac{1}{\sqrt{15}} & 0 & 0 & 0 & \sqrt{\frac{6}{35}} \\ 0 & 0 & 0 & 0 & 0 & -\frac{1}{\sqrt{5}} & 0 & 0 & \sqrt{\frac{3}{14}} & \frac{1}{\sqrt{70}} \\ 0 & 0 & 0 & 0 & 0 & 0 & 0 & \sqrt{\frac{3}{14}} & 0 & 0 \\ 0 & 0 & 0 & 0 & 0 & 0 & \sqrt{\frac{6}{35}} & \frac{1}{\sqrt{70}} & 0 & 0 \end{pmatrix}.$$

Let $A^n = A^{(1)}n_1(x) + A^{(2)}n_2(x)$. One can verify that A^n satisfies $A^n = (O^n)^{\mathrm{T}} A^{(1)} O^n$ with

$$O^n = \begin{pmatrix} \cos(\theta) & 0 & 0 & 0 & 0 & \sin(\theta) & 0 & 0 & 0 & 0 \\ 0 & \cos(2\theta) & 0 & 0 & 0 & 0 & 0 & -\sin(2\theta) & 0 & 0 \\ 0 & 0 & \cos(\theta) & 0 & 0 & 0 & 0 & 0 & 0 & \sin(\theta) \\ 0 & 0 & 0 & \cos(3\theta) & 0 & 0 & 0 & 0 & \sin(3\theta) & 0 \\ 0 & 0 & 0 & 0 & 1 & 0 & 0 & 0 & 0 & 0 \\ -\sin(\theta) & 0 & 0 & 0 & 0 & \cos(\theta) & 0 & 0 & 0 & 0 \\ 0 & 0 & 0 & 0 & 0 & 0 & 1 & 0 & 0 & 0 \\ 0 & \sin(2\theta) & 0 & 0 & 0 & 0 & 0 & \cos(2\theta) & 0 & 0 \\ 0 & 0 & 0 & -\sin(3\theta) & 0 & 0 & 0 & 0 & \cos(3\theta) & 0 \\ 0 & 0 & -\sin(\theta) & 0 & 0 & 0 & 0 & 0 & 0 & \cos(\theta) \end{pmatrix}$$

where θ is the angle measured in the anti-clockwise sense between the normal vector $n(x)$ and the x_1 direction. The right hand side matrix (P) is a diagonal negative semi-definite matrix with all the entries depending upon the material parameters [6, 13]. Thus P_3 equations satisfy assumption 2.

C. Similarities to the general framework

1. Trivially follows from the definition of the flux's Jacobians (27)

$$\left(A_M^{(i)}\right)^{\mathrm{T}} = \left(\int_{\mathbb{R}^d} \Psi_M \xi_i \left(\Psi_M\right)^{\mathrm{T}} f_0 d\xi\right)^{\mathrm{T}} = \int_{\mathbb{R}^d} \Psi_M \xi_i \left(\Psi_M\right)^{\mathrm{T}} f_0 d\xi = A_M^{(i)}.$$

2. Orthogonality (24a) and recursion (24b) of Hermite polynomials provides [33]

$$\left\langle \Psi_M^e f_0, \xi_1 \left(\Psi_M^e\right)^{\mathrm{T}} f_0 \right\rangle_K = 0_{\Xi_e^M \times \Xi_e^M}, \quad \left\langle \Psi_M^o f_0, \xi_1 \left(\Psi_M^o\right)^{\mathrm{T}} f_0 \right\rangle_K = 0_{\Xi_o^M \times \Xi_o^M}. \tag{56}$$

From the definition of $A_M^{(1)}$ in (27) and the ordering $\Psi_M = \left(\left(\Psi_M^o\right)^{\mathrm{T}}, \left(\Psi_M^e\right)^{\mathrm{T}}\right)^{\mathrm{T}}$ in definition 3.3 we find

$$A_M^{(1)} = \begin{pmatrix} \left\langle \Psi_M^o f_0, \xi_1 \left(\Psi_M^o\right)^{\mathrm{T}} f_0 \right\rangle_K & \left\langle \Psi_M^o f_0, \xi_1 \left(\Psi_M^e\right)^{\mathrm{T}} f_0 \right\rangle_K \\ \left\langle \Psi_M^e f_0, \xi_1 \left(\Psi_M^o\right)^{\mathrm{T}} f_0 \right\rangle_K & \left\langle \Psi_M^e f_0, \xi_1 \left(\Psi_M^e\right)^{\mathrm{T}} f_0 \right\rangle_K \end{pmatrix} = \begin{pmatrix} 0_{\Xi_o^M \times \Xi_o^M} & A_\Psi^{(M,M)} \\ \left(A_\Psi^{(M,M)}\right)^{\mathrm{T}} & 0_{\Xi_e^M \times \Xi_e^M} \end{pmatrix}$$

where the last equality is a consequence of (56) and the definition of $A_\Psi^{(M,M)}$ given in definition 3.4.

3. From the definition of $A_\Psi^{(M,M)}$ and $A_\psi^{(M,M-1)}$ (definition 3.4), we conclude that

$$A_\Psi^{(M,M)} = \left(A_\Psi^{(M,M-1)}, A_\psi^{(M,M)}\right),$$

where $A_\Psi^{(M,M-1)}$ is a square invertible matrix [32]. This implies that $A_\Psi^{(M,M)}$ has full rank and since $\Xi_o^M \leq \Xi_e^M$ we have $\mathrm{rank}(A_\Psi^{(M,M)}) = \Xi_o^M$.

4. From the definition of $A_M^{(i)}$ (27) we find

$$A_M^n = \sum_{i=1}^{d} A_M^{(i)} n_i^{(1)}(x) = \int_{\mathbb{R}^d} \Psi_M(\xi) \xi_i n_i^{(1)} \left(\Psi_M(\xi)\right)^{\mathrm{T}} f_0(\xi) d\xi,$$

where $n^{(1)}(x)$ is the same as $n(x)$ but relabelled for convenience. The normal vector $n^{(1)}(x)$ can be used to define a local coordinate system. Let the d mutually orthogonal axis of this coordinate system be represented by a set of d orthogonal unit vectors $\{n^{(1)}(x), \ldots, n^{(d)}(x)\}$ where $n^{(i)} \in \mathbb{R}^d, \forall i \in \{1, 2, \ldots, d\}$. In these local coordinates we represent the velocity through $\xi^n \in \mathbb{R}^d$ where $\xi_i^n = \xi_j n_j^{(i)}$. The velocity in Cartesian coordinates (ξ) can be related to the velocity in local coordinates (ξ^n) through an orthogonal rotation matrix $O^n \in \mathbb{R}^{d \times d}$

$$O^n \xi^n = \xi.$$

With the above relation, the expression for A_M^n can be simplified to

$$\begin{aligned} A_M^n &= \int_{\mathbb{R}^d} \Psi_M(O^n\xi^n) \xi_1^n \left(\Psi_M(O^n\xi^n)\right)^{\mathrm{T}} f_0(O^n\xi^n) |\det(O^n)| d\xi^n \\ &= \left(\hat{O}_M^n\right)^{\mathrm{T}} \left(\int_{\mathbb{R}^d} \Psi_M(\xi^n) \xi_1^n \left(\Psi_M(\xi^n)\right)^{\mathrm{T}} f_0(\xi^n) d\xi^n\right) \hat{O}_M^n, \end{aligned}$$

where $d\xi^n$ represents a volume element in local coordinates and for the last equality we have used $|\det(O^n)|= 1$ and $f_0(\xi^n) = f_0(O^n\xi^n)$. For the last equality we have used the rotational property of Ψ_M (28). Since a change of notation does not influence an integral, we find

$$\int_{\mathbb{R}^d} \Psi_M(\xi^n)\xi_1^n \left(\Psi_M(\xi^n)\right)^{\mathrm{T}} f_0(\xi^n)d\xi^n = \int_{\mathbb{R}^d} \Psi_M(\xi)\xi_1 \left(\Psi_M(\xi)\right)^{\mathrm{T}} f_0(\xi)d\xi = A_M^{(1)}$$

which then implies $A_M^n = \left(\hat{O}_M^n\right)^{\mathrm{T}} A_M^{(1)}\hat{O}_M^n$.

5. Semi-negative definiteness of P_M is a result of the semi-negative definiteness of Q (21) and the definition of P_M (27): $\left(\Lambda_M(r)\right)^{\mathrm{T}} P_M\Lambda_M(r) = \frac{1}{\mathrm{Kn}}\left\langle r, Q(r)\right\rangle_K \leq 0, \quad \forall \quad r \in K.$

D. Stability of weak kinetic boundary implementation

Choosing $\phi = f_M^h(\cdot,t,\cdot)$ in (40) and integrating by parts, we find

$$\begin{aligned}\frac{1}{2}\partial_t\|f_M^h(t)\|_X^2+\frac{1}{2}\oint_{\partial\Omega_h}\int_{\mathbb{R}^d}\xi_i n_i\left(f_M^h(t)\right)^2 f_0^{-1}d\xi ds = \frac{1}{\mathrm{Kn}}\int_{\Omega_h}\int_{\mathbb{R}^d} f_M^h(t)Q(f_M^h(t))f_0^{-1}d\xi dx \\ + \oint_{\partial\Omega_h}\int_{\xi_i n_i<0}\xi_i n_i\left(f_M^h(t)-f_{in}(t)\right)f_M^h(t)f_0^{-1}d\xi ds,\end{aligned} \tag{57}$$

where we assume that all integrals are exact. Trivially,

$$-\oint_{\partial\Omega_h}\int_{\xi_i n_i>0}\xi_i n_i\left(f_M^h(t)\right)^2 f_0^{-1}d\xi ds \leq 0, \quad \forall \quad t\in[0,T].$$

Using the above inequality and the dissipation property of Q given in (21) in the estimate (57), we find

$$\begin{aligned}\partial_t\|f_M^h(t)\|_X^2 &\leq \oint_{\partial\Omega_h}\int_{\xi_i n_i<0}\xi_i n_i\left(f_M^h(t)\right)^2 f_0^{-1}d\xi ds - 2\oint_{\partial\Omega_h}\int_{\xi_i n_i<0}\xi_i n_i f_{in}(t)f_M^h(t)f_0^{-1}d\xi ds \\ &= \underbrace{\oint_{\partial\Omega_h}\int_{\xi_i n_i<0}\xi_i n_i\left(f_M^h(t)-f_{in}(t)\right)^2 f_0^{-1}d\xi ds}_{\leq 0} - \oint_{\partial\Omega_h}\int_{\xi_i n_i<0}\xi_i n_i\left(f_{in}(t)\right)^2 f_0^{-1}d\xi ds, \\ &\leq -\oint_{\partial\Omega_h}\int_{\xi_i n_i<0}\xi_i n_i\left(f_{in}(t)\right)^2 f_0^{-1}d\xi ds.\end{aligned}$$

Integrating the above inequality over $[0,T]$ provides the result.

E. Kinetic flux implementation

Using the definition of $V_{h,M}$, we express f_M^h as

$$f_M^h(x,t,\xi) = \Lambda_M(f_M^h(x,t,\cdot))\cdot\Psi_M(\xi)f_0(\xi)$$

where $\Lambda_M(f_M^h(x,t,\cdot)) \in V_h$. Replacing the above expansion in (40), we find

$$\begin{aligned}\int_{\Omega_h}\phi^{\mathrm{T}}\partial_t\Lambda_M(f_M^h(t))dx+\sum_{i=1}^d\int_{\Omega_h}\phi^{\mathrm{T}}A_M^{(i)}\partial_{x_i}\Lambda_M(f_M^h(t))dx - \int_{\Omega_h}\phi^{\mathrm{T}}P_M\Lambda_M(f_M^h(t))dx \\ = \frac{1}{2}\oint_{\partial\Omega_h}\phi^{\mathrm{T}}\left(A_M^n - D_M^n\right)\left(\Lambda_M(f_M^h(t))-\Lambda_M(f_{in}(t))\right)ds, \ \forall\ \phi\in V_h.\end{aligned} \tag{58}$$

Performing integration-by-parts on every element of Ω_h separately, we find

$$\sum_{i=1}^{d}\int_{\Omega_h}\phi^{\mathrm{T}}A_M^{(i)}\partial_{x_i}\Lambda_M(f_M^h(t))dx=\sum_{\kappa\in\Omega_h}\sum_{i=1}^{d}\int_{\kappa}\phi^{\mathrm{T}}A_M^{(i)}\partial_{x_i}\Lambda_M(f_M^h(t))dx$$
$$=\sum_{\kappa\in\Omega_h}\left(\oint_{\partial\kappa}\phi^{\mathrm{T}}A_M^{n_\kappa}\Lambda_M^{(\kappa,+)}ds-\int_{\kappa}(\partial_{x_i}\phi)^T\,A_M^{(i)}\Lambda_M(f_M^h(t))dx\right).$$

Continuity of functions in the approximation space V_h implies $\Lambda_M^{(\kappa,+)}=\Lambda_M^{(\kappa,-)}$ which allows us to write

$$\oint_{\partial\kappa}\phi^{\mathrm{T}}A_M^{n_\kappa}\Lambda_M^{(\kappa,+)}ds=\oint_{\partial\kappa}\phi^{\mathrm{T}}\underbrace{\frac{1}{2}\left(A_M^{n_\kappa}\left(\Lambda_M^{(\kappa,+)}+\Lambda_M^{(\kappa,-)}\right)+D_M^{n_\kappa}\left(\Lambda_M^{(\kappa,+)}-\Lambda_M^{(\kappa,-)}\right)\right)}_{=\mathcal{F}(\Lambda_M^{(\kappa,+)},\Lambda_M^{(\kappa,-)};n^\kappa)}ds$$

Using the above relation in (58) provides us with the result.

F. Discrete Velocity Method

All of our test cases involve a 2D physical space for which the linearised BE (19) reduces to

$$\partial_t f+\sum_{i=1}^{2}\xi_i\partial_{x_i}f=Q(f). \tag{59}$$

All the macroscopic quantities in (20) can be recovered using the following projections of f along the ξ_3 direction

$$g=\int_{\mathbb{R}}He_0(\xi_3)f d\xi_3,\quad h=\int_{\mathbb{R}}He_2(\xi_3)f d\xi_3,$$

where He_i denotes a Hermite polynomial of i-th degree. We are interested in macroscopic quantities therefore we only solve for g and h that reduces the computational cost of solving (59). Testing (59) with He_0 and He_2 provides the governing equations for g and h

$$\partial_t g+\sum_{i=1}^{2}\xi_i\partial_{x_i}g=\int_{\mathbb{R}}He_0Q(f)d\xi_3,\quad \partial_t h+\sum_{i=1}^{2}\xi_i\partial_{x_i}h=\int_{\mathbb{R}}He_2Q(f)d\xi_3. \tag{60}$$

We solve both the above equations using a DVM described in the text.

References

[1] Abdelmalik, M. and Brummelen, H. v. (2016). An entropy stable discontinuous Galerkin finite-element moment method for the Boltzmann equation. *Computers & Mathematics with Applications*, 72(8):1988 – 1999. Finite Elements in Flow Problems 2015.

[2] Abdelmalik, M. and Brummelen, H. v. (2017). Error estimation and adaptive moment hierarchies for goal-oriented approximations of the Boltzmann equation. *Computer Methods in Applied Mechanics and Engineering*, 325(Supplement C):219 – 239.

[3] Baranger, C., Claudel, J., Hérouard, N., and Mieussens, L. (2014). Locally refined discrete velocity grids for stationary rarefied flow simulations. *Journal of Computational Physics*, 257:572 – 593.

[4] Beckmann, A. F., Rana, A. S., Torrilhon, M., and Struchtrup, H. (2018). Evaporation boundary conditions for the linear R13 equations based on the Onsager theory. *Entropy*, 20(9).

[5] Bird, G. A. (1995). *Molecular gas dynamics and the direct simulation of gas flows*. Oxford : Clarendon Press, repr. (with corrections) edition.

[6] Brunner, T. A. and Holloway, J. P. (2005). Two-dimensional time dependent Riemann solvers for neutron transport. *Journal of Computational Physics*, 210(1):386 – 399.

[7] Cai, Z., Fan, Y., and Li, R. (2014). Globally hyperbolic regularization of Grad's moment system. *Communications on Pure and Applied Mathematics*, 67(3):464–518.

[8] Cai, Z. and Li, R. (2010). Numerical regularized moment method of arbitrary order for Boltzmann-BGK equation. *SIAM Journal on Scientific Computing*, 32(5):2875–2907.

[9] Cai, Z. and Torrilhon, M. (2017). Numerical simulation of microflows using moment methods with linearized collision operator. *Journal of Scientific Computing*.

[10] Carpenter, M. H., Gottlieb, D., and Abarbanel, S. (1994). Time-stable boundary conditions for finite-difference schemes solving hyperbolic systems: Methodology and application to high-order compact schemes. *Journal of Computational Physics*, 111(2):220 – 236.

[11] Cercignani, C. (1988). *The Boltzmann Equation and Its Applications*. Springer, 67 edition.

[12] Fernández, D. C. D. R., Hicken, J. E., and Zingg, D. W. (2014). Review of summation-by-parts operators with simultaneous-approximation-terms for the numerical solution of partial differential equations. *Computers and Fluids*, 95:171 – 196.

[13] Frank, M., Hauck, C., and Küpper, K. (2016). Convergence of filtered spherical harmonic equations for radiation transport. *Commun. Math. Sci*, 14(5):1443–1465.

[14] Grad, H. (1949). On the kinetic theory of rarefied gases. *Communications on Pure and Applied Mathematics*, 2(4):331–407.

[15] Grad, H. (1962). Asymptotic theory of the Boltzmann equation. II. *Pros. 3rd Internat. Sympos., Palais de l'UNESCO, Paris, 1962*, 1:26–59.

[16] Grad, H. (1963). Asymptotic theory of the Boltzmann equation. *The Physics of Fluids*, 6(2):147–181.

[17] Gupta, V. K. and Torrilhon, M. (2014). Higher order moment equations for rarefied gas mixtures. *Proceedings of the Royal Society of London A: Mathematical, Physical and Engineering Sciences*, 471(2173).

[18] Gustafsson, B., Kreiss, H.-O., and Oliger, J. (1995). *Time dependent problems and difference methods*. John Wiley and Sons, Inc.

[19] Harten, A. (1983). On the symmetric form of systems of conservation laws with entropy. *Journal of Computational Physics*, 49(1):151 – 164.

[20] Kreiss, H.-O. and Scherer, G. (1974). Finite element and finite difference methods for hyperbolic partial differential equations. In de Boor, C., editor, *Mathematical Aspects of Finite Elements in Partial Differential Equations*, pages 195 – 212. Academic Press.

[21] Kreiss, H.-O. and Wu, L. (1993). On the stability definition of difference approximations for the initial boundary value problem. *Applied Numerical Mathematics*, 12(1):213 – 227. Special Issue.

[22] Levermore, C. D. (1996). Moment closure hierarchies for kinetic theories. *Journal of Statistical Physics*, 83(5):1021–1065.

[23] Mandal, J. and Deshpande, S. (1994). Kinetic flux vector splitting for Euler equations. *Computers and Fluids*, 23(2):447 – 478.

[24] Mieussens, L. (2000). Discrete-velocity models and numerical schemes for the Boltzmann-BGK equation in plane and axisymmetric geometries. *Journal of Computational Physics*, 162(2):429 – 466.

[25] Nordström, J. (2016). A roadmap to well posed and stable problems in computational physics. *Journal of Scientific Computing*, pages 1–21.

[26] Nordström, J. and Wahlsten, M. (2015). Variance reduction through robust design of boundary conditions for stochastic hyperbolic systems of equations. *Journal of Computational Physics*, 282:1 – 22.

[27] Parsani, M., Carpenter, M. H., and Nielsen, E. J. (2015). Entropy stable wall boundary conditions for the three-dimensional compressible Navier-Stokes equations. *Journal of Computational Physics*, 292:88 – 113.

[28] Rana, A., Torrilhon, M., and Struchtrup, H. (2013). A robust numerical method for the R13 equations of rarefied gas dynamics: Application to lid driven cavity. *Journal of Computational Physics*, 236(1):169–186.

[29] Rana, A. S. and Struchtrup, H. (2016). Thermodynamically admissible boundary conditions for the regularized 13 moment equations. *Physics of Fluids*, 28(2):027105.

[30] Ringhofer, C., Schmeiser, C., and Zwirchmayr, A. (2001). Moment methods for the semiconductor Boltzmann equation on bounded position domains. *SIAM Journal on Numerical Analysis*, 39(3):1078–1095.

[31] Sarna, N., Giesselmann, J., and Torrilhon, M. (2018). Convergence analysis of the Grad's Hermite approximation to the Boltzmann equation. *arXiv:1809.08213*.

[32] Sarna, N. and Torrilhon, M. (2018a). Entropy stable Hermite approximation of the linearised Boltzmann equation for inflow and outflow boundaries. *Journal of Computational Physics*, 369:16 – 44.

[33] Sarna, N. and Torrilhon, M. (2018b). On stable wall boundary conditions for the Hermite discretization of the linearised Boltzmann equation. *Journal of Statistical Physics*, 170(1):101–126.

[34] Seibold, B. and Frank, M. (2014). Starmap—a second order staggered grid method for spherical harmonics moment equations of radiative transfer. *ACM Trans. Math. Softw.*, 41(1):4:1–4:28.

[35] Struchtrup, H. (2010). *Macroscopic transport equations for rarefied fas flows*. Springer Ltd.

[36] Struchtrup, H., Beckmann, A., Rana, A. S., and Frezzotti, A. (2017). Evaporation boundary conditions for the R13 equations of rarefied gas dynamics. *Physics of Fluids*, 29(9):092004.

[37] Struchtrup, H. and Torrilhon, M. (2007). H-theorem, regularization, and boundary conditions for linearized 13 moment equations. *Phys. Rev. Lett.*, 99:014502.

[38] Su, W., Lindsay, S., Liu, H., and Wu, L. (2017). Comparative study of the discrete velocity and lattice Boltzmann methods for rarefied gas flows through irregular channels. *Phys. Rev. E*, 96:023309.

[39] Svärd, M., Carpenter, M. H., and Nordström, J. (2007). A stable high-order finite difference scheme for the compressible Navier-Stokes equations, far-field boundary conditions. *Journal of Computational Physics*, 225(1):1020 – 1038.

[40] Svärd, M. and Nordström, J. (2014). Review of summation-by-parts schemes for initial boundary-value problems. *Journal of Computational Physics*, 268:17 – 38.

[41] Tang, H. (2004). Kinetic flux vector splitting for the Euler equations with general pressure laws. *Journal of Computational Mathematics*, 22(4):622–632.

[42] Thatcher, T., Zheng, Y., and Struchtrup, H. (2008). Boundary conditions for Grad's 13 moment equations. *Progress in Computational Fluid Dynamics, an International Journal*, 8(1-4):69–83.

[43] Torrilhon, M. (2015). Convergence study of moment approximations for boundary value problems of the Boltzmann-BGK equation. *Communications in Computational Physics*, 18(03):529–557.

[44] Torrilhon, M., Au, J., and Struchtrup, H. (2003). Explicit fluxes and productions for large systems of the moment method based on extended thermodynamics. *Continuum Mechanics and Thermodynamics*, 15(1):97–111.

[45] Torrilhon, M. and Sarna, N. (2017). Hierarchical Boltzmann simulations and model error estimation. *Journal of Computational Physics*, 342:66 – 84.

[46] Wang, S. and Kreiss, G. (2017). Convergence of summation-by-parts finite difference methods for the wave equation. *Journal of Scientific Computing*, 71(1):219–245.

[47] Yang, B., Flusser, J., and Kautsky, J. (2018). Rotation of 2D orthogonal polynomials. *Pattern Recognition Letters*, 102:44 – 49.